Formation and evolution of clumpy tidal tails around globular clusters

R. Capuzzo Dolcetta

dolcetta@uniroma1.it

P. Di Matteo

p.dimatteo@uniroma1.it

and

P. Miocchi

miocchi@uniroma1.it

Dep. of Physics, Universitá di Roma La Sapienza, P.le Aldo Moro 2, 00185 Rome, Italy

ABSTRACT

We present some results of numerical simulations of a globular cluster orbiting in the central region of a triaxial galaxy on a set of 'loop' orbits. Tails start forming after about a quarter of the globular cluster orbital period and develop, in most cases, along the cluster orbit, showing clumpy substructures as observed, for example, in Palomar 5. If completely detectable, clumps can contain about $7000 M_\odot$ each, i.e. about 10% of the cluster mass at that epoch. The morphology of tails and clumps and the kinematical properties of stars in the tails are studied and compared with available observational data. Our finding is that the stellar velocity dispersion tends to level off at large radii, in agreement to that found for M15 and ω Centauri.

Subject headings: methods: n-body simulations, globular clusters: general, galaxies: kinematics and dynamics

1. Introduction

Since Shapley's pioneering work (Shapley 1918), globular clusters (GCs) have played a key-role in our understanding of the Universe and of the manner in which our Galaxy

formed: in the Milky Way they are the oldest stellar systems found, with ages in the range 12 to 15 Gyr, so to represent tracers of the early formation history of the Galaxy.

They are the best systems to study stellar dynamics, having relaxation times smaller than their age, so that, at least in the core, stars are expected to have lost memory of their initial conditions (Binney and Tremaine 1987). In the early 1980s a number of approximated numerical studies of spherical self-gravitating systems (Cohn 1980) showed that the central density tends to increase dramatically over the time, so that ultimately a central power-law cusp is produced in the central region, even if these systems have an early evolutionary phase that resembles the King sequence of cluster models (King 1966). Together with the slow collapse of the core, star evaporation occurs: the approach to equipartition implies that the more massive stars sink toward the center of the cluster, while lighter stars expand their orbit. Core collapse can be halted by the presence of hard binaries which, acting as energy sources, heat the central core by 3-bodies encounters (Hènon 1961; Ostriker 1985).

Internal processes are not the only responsible of dynamical evolution in these systems: perturbations due to an external field (in particular, shocks due to the passage through the galactic disk and to the interaction with the bulge) can accelerate significantly the evolution of a globular cluster. Indeed, it is commonly accepted that the present globular cluster population represents the survivor of an initially more numerous one, depauperated by many disruptive processes (Murali & Weinberg 1997a,b; Fall & Zhang 2001).

There is observational evidence that the globular cluster system (GCS) radial profile is less peaked than that of halo stars in our galaxy, M31 (Capuzzo Dolcetta & Vignola 1997), M87 and M49 (Grillmair et al. 1986; McLaughlin 1995), as well as in three galaxies of the Fornax cluster (Capuzzo Dolcetta & Donnarumma 2001) and of 11 elliptical galaxies (Capuzzo Dolcetta & Tesseri 1999). This fact leads to the hypothesis (Capuzzo Dolcetta & Tesseri 1997) that the two systems (halo and GCS) originally had the same profile and that, afterwards, the GCS evolved mainly due to two complementary effects: tidal interaction with the galactic field (which causes less concentrated clusters to disintegrate more rapidly) and dynamical friction (which induces massive globular clusters to decay in the central galactic region in less than 10^8 years, see Capuzzo Dolcetta & Vicari (2003)). External tidal fields have the effect of inducing the evolution of the shape of the mass function of individual clusters, because of the preferential depletion of low-mass stars (Baumgardt & Makino 2003) as a consequence of two-body relaxation . Strong evidence that the tidal field plays a fundamental role in the evolution of mass functions was achieved by the discovery that their slopes correlate more strongly with the cluster location in the Milky Way than with the cluster metallicity (Djorgovski et al. 1993).

In the last decade, many observational evidences of the interaction of GCs with the tidal field have been found. Firstly, Grillmair et al. (1995), using colour-magnitude selected star counts in a dozen of galactic GCs, showed that in the outer parts of these clusters the stellar

surface density profiles exceeded the prediction of King models, extending also outside the tidal radius of the corresponding King model. Other results confirmed Grillmair's findings (Lehmann & Scholz 1997; Testa et al. 2000; Leon et al. 2000; Siegel et al. 2001; Lee et al. 2003); all these works suggest that many GCs are likely surrounded by haloes or tails, made up of stars which were tidally stripped from the system. This was the state of the art until the spectacular findings of two tidal tails emanating from the outer part of the Palomar 5 globular cluster and covering an arc of 10 degrees on the sky, corresponding to a projected lenght of 4 kpc at the distance of the cluster (Odenkirchen et al. 2001, 2003), obtained in the framework of the Sloan Digital Sky Survey Project (see also *http://www.sdss.org*).

One of the relevant observational features of Palomar 5 is the presence of well defined clumps in the star distribution along the tails (Odenkirchen et al. 2001, 2003). Also NGC 6254 and Palomar 12 seem to show clumpy structures in their tails (Leon et al. 2000). This still deserves an exaustive interpretation. Actually, the simulations of Combes et al. (1999) show the presence of small clumps (containing about 0.5% of the total number of stars of the cluster) in the tidal tails. The authors attribute the formation of these clumps to strong gravitational shocks suffered by the cluster. On another hand, Dehnen et al. (2004) were not able to reproduce the clumps observed in the tails of Pal 5, even adopting a realistic galactic model, so that they argued that these structures could be due to the effect of Galactic sub-structures not accounted in their simulations (giant molecular clouds, spiral arms, dark-matter sub-halos or massive compact halo objects).

With the aim of understanding better the mechanism of interaction of GCs with the external field, in particular with the bulge, and to investigate on the presence of clumps in tidal tails, we performed numerical simulations of globular clusters in orbit in a triaxial galaxy, aiming also at clarifying the morphological connection between the clusters tidal tails and their orbits.

In the next sections we show the results for globular clusters on 'loop' orbits in an inner region of a triaxial galaxy. In particular, in Sect.2, an overview of the numerical methods adopted to perform the simulation are discussed; in Sect.3 the galaxy and cluster model adopted are presented; in Sect.4 and Sect.5 we deal with the main results of our work, especially that concerning the formation of tidal tails around the cluster and their orientation respect to the cluster orbit (Sect.4.1), the radial density profiles of the cluster, as they evolve with time, and the presence of clumpy regions in the tails (Sect.4.2), the velocity dispersion of stars in the cluster (Sect.4.3), the estimate of the mass loss rate (Sect.5.1) and the evolution of the global mass functions (Sect.5.2); in the last section all the findings are summarized and discussed.

2. Numerical method

All the simulations were performed by means of an implementation of a *tree-code* carried out mainly by one of the authors (P.M.). It is based on the algorithm described in Barnes & Hut (1986) and adopts multipolar expansions of the potential truncated at the quadrupole moment. It was parallelized to run on high performance computers via MPI routines, employing an original parallelization approach (Miocchi & Capuzzo-Dolcetta 2002). The time-integration of the 'particles' trajectories is performed by a 2nd order leap-frog algorithm. This latter uses individual and variable time-steps according to the block-time scheme (Aarseth 1985; Hernquist & Katz 1989), in addition with corrections implemented in order to keep the same order of approximation also during the time-step change. The maximum time-step allowed is $\Delta t_{\text{max}} = 0.01 t_{\text{c}}$ (where $t_{\text{c}} \sim (r_{\text{core}}^3/GM)^{1/2}$ is the core-crossing time of the GC, being M its mass and r_{core} the core radius), while the minimum is $\Delta t_{\text{min}} = \Delta t_{\text{max}}/2^8$, thus fastest particles may have a time-step as small as $\sim 4 \times 10^{-5} t_{\text{c}}$. The best criterion we found for choosing the time-step of the i-th particle is via the formula: $\min\{(d_i/a_i)^{1/2}, d_i/v_i\}/20$, where v_i is the velocity of the particle relative to its first neighbour, d_i the distance from its first neighbour and a_i the modulus of the acceleration.

To avoid instability in the time-integration, we smoothed the $1/r_{ij}$ interaction potential by substiuting $1/r_{ij}$ with a continuous β-spline function that gives an exactly Newtonian potential for $r_{ij} > \epsilon$ and a force that vanishes for $r_{ij} \to 0$ (Hernquist & Katz 1989). In all the runs we set $\epsilon = 1.4 \times 10^{-3} r_{core}$, so to have $(\epsilon^3/GM)^{1/2} \sim \Delta t_{\text{min}}$. Note that such value of ϵ is much less than the typical interparticle distance. As regards the quality of the orbits time–integration, we checked that the upper bound of the relative error in the energy conservation ($\Delta E/E$) is 10^{-8} per time–step, even in absence of the external field.

3. Cluster and galaxy models

3.1. Galaxy model

The external galactic field due to the bulge is represented by the potential of the Schwarzschild model (Schwarzschild 1979). The Schwarzschild model is a non-rotating, self-consistent triaxial ellipsoid with axis ratios $2 : 1.25 : 1$, typical of many galaxies (Bertola et al. 1991).
Defining adimensional units as

$$x' = x/r_b, \quad y' = y/r_b, \quad z' = z/r_b, \tag{1}$$

r_b being the bulge core radius, the potential $\Phi(x', y', z')$ is expressed as the sum of a spherically simmetric term, $\Phi_{r'}(r')$, $(r' = r/r_b)$, which corresponds to the potential given by a density distribution following the modified Hubble's law $\rho(r') = \rho_0 \left[1 + (r')^2\right]^{-3/2}$, $(\rho_0 \equiv M_b/r_b^3)$, plus two spherical armonics, $\Phi_1(z', r')$ and $\Phi_2(x', y', r')$:

$$\Phi(x', y', z') = A[\Phi_{r'}(r') + \Phi_1(z', r') + \Phi_2(x', y', r')], \tag{2}$$

where

$$\Phi_{r'} = -\frac{1}{r'} \ln\left[r' + \sqrt{1 + (r')^2}\right], \tag{3}$$

$$\Phi_1 = c_1 \frac{3(z')^2 - (r')^2}{2(1 + c_2 (r')^2)^{3/2}}, \tag{4}$$

$$\Phi_2 = -3c_3 \frac{(x')^2 - (y')^2}{(1 + c_4 (r')^2)^{3/2}}, \tag{5}$$

$$A = 4\pi \frac{GM_b}{r_b}, \tag{6}$$

and M_b is the bulge mass.

The coefficients c_i have the values: $c_1 = 0.06408$, $c_2 = 0.65456$, $c_3 = 0.01533$, $c_4 = 0.48067$ (de Zeeuw & Merritt 1983; Pesce et al. 1992). They have been determined so to have density axial ratios roughly constant with r.

Following Pesce et al. (1992), we will consider $M_b = 3 \times 10^9$ M$_\odot$ and $r_b = 200$ pc, but the results obtained in adimensional variables (see Appendix A) are scalable in terms of r_b and M_b, for given initial conditions for positions, velocities and m_i/M_b.

3.2. Cluster model

As initial cluster model, we chose a multimass King distribution (King 1966; Da Costa & Freeman 1976), with 10 mass classes, ranging between 0.12 and 1.2M$_\odot$ and equally spaced in a logarithmic scale. To find the distribution function for each mass class, we integrated the Poisson's equation as described in the Appendix B.

The initial cluster mass function is chosen in the Salpeter form (Salpeter 1955), i.e. $dN/dm \propto m^{-2.35}$ (see Appendix C for a discussion about the remnants of progenitor stars more massive than 1.2M$_\odot$). We included mass segregation in the initial conditions of our cluster model because we wanted to simulate a dynamically-relaxed cluster (supposed to be sufficiently massive to have frictionally decayed in the central galactic region). The "initial" mass of the system is $M_{tot} = 3 \times 10^5$ M$_\odot$ $= 10^{-4}M_b$, the initial concentration parameter is $c = log(r_t/r_{\rm core}) = 1.1$ and the central velocity dispersion is $\sigma = 9.4$ km s^{-1} $= 0.036 \times r_b/t_{cross}$,

being $t_{cross} = (r_b^3/GM_b)^{1/2}$ the bulge crossing time.

Then, the system was represented by a number (N) of 'particles' lower than the number of stars in the real cluster, with masses properly rescaled such to give a total mass equal to M_{tot}. The cluster moves on the y-z coordinate plane, following loop orbits of different ellipticity

$$e = \frac{R_a - R_p}{R_a + R_p},\tag{7}$$

being R_a and R_p, respectively, the apocenter and pericenter distances (see Table 1 for orbital parameters).

4.   Results on tidal tails

In the following, we present the main findings of our work concerning with tidal tails structure and evolution. When we refer to the center-of-density of the cluster, we mean a mass density-weighted center as defined by Casertano & Hut (1985).

4.1.   Tidal tails formation and morphology

In all the simulations performed, the cluster starts moving around the galaxy center in a clockwise direction (seen from the positive x axis). The different loop orbits have been followed for about 30 t_{cross}.

In Fig.1, 2, 3, 4, 5, 6, 7 and 8, the formation and subsequent development of tails around the globular cluster is shown.

After about 8 t_{cross}, tidal tails are clearly formed. They continuosly accrete by stars leaving the cluster, so that after 30 t_{cross}, in the case of quasi-circular orbit ($e = 0.03$), they are elongated for more than 3 r_b each and contain about 75% of the initial cluster mass. As it is clearly visible from these figures, the degree of elongation of the tails along the cluster orbital path strongly depends on the ellipticity e (Eq.7) of the cluster orbit. Indeed, while in the case of the quasi-circular orbit tails are a clear tracer of the cluster path, in the most eccentric orbit ($e = 0.57$), tails are strictly elongated along the orbital path only when the cluster is near the perigalacticon, while at the apogalacticon they tend to deviate from the cluster path. Nevertheless, in Miocchi et al. (2004) a remarkable tails—orbit alignment is found for clusters moving on quasi–radial orbits in the same bulge potential. However, it is important to stress that, in order to perform accurate predictions of the cluster orbit from observational detections of tidal tails, it is necessary to look at the spatial distribution of stars well outside the cluster (typically $2 - 3$ times the cluster limiting radius). Indeed, in

the vicinity of the globular cluster, stars in the tails are not aligned with the cluster orbit, neither in the case of small ellipticity (see Fig.9), but they distribute along the peculiar $S-$shape profile not aligned along the orbit.

The orbit ellipticity also influences the similarity between the two cluster tails. For the quasi-circular orbit, these structures are simmetric for the whole duration of the simulation, being elongated, at a given time, for the same length. For more eccentric orbits, the leading tail tends to be more elongated than the trailing one when going from the apocenter to the orbital pericenter and, viceversa, it is less elongated than the trailing tail when the cluster moves towards the apocenter. In any case, the tail that precedes the cluster extends always slightly below the orbit while the trailing one lies slighlty above this latter, in agreement with what observed for Palomar 5.

The shape and orientation of the tails can be easily understood in the case of a cluster moving on a circular orbit in an axysimmetric external field, using a rotating frame of reference with the origin in the baricentre of the cluster, with the X-axis pointing towards the galactic center, the Y-axis parallel to the direction of motion of the cluster and the Z-axis orthogonal to the orbital plane. In this reference frame, the galactic tidal field tends to accelerate stars along the $\pm X$ directions (Heggie & Hut 2003), making stars to escape from the system through the Lagrangian points L_1 and L_2 (which are the two equilibrium points located along the X-axis). But the Coriolis acceleration tends to align escaping stars along the direction of motion of the cluster around the galaxy, this yelding the peculiar S-shape just outside the cluster, in the inner part of the tails.

4.2. Density profiles

In order to describe the tidal debris and to compare our findings with observations (Lehmann & Scholz 1997; Testa et al. 2000; Leon et al. 2000; Siegel et al. 2001; Lee et al. 2003; Odenkirchen et al. 2003), we studied the radial profile of the volume and surface densities (azimutally averaged) as a function of the distance from the cluster center. Obviously, this description does not take into account the fact that stars lost from the cluster are not placed in a spherically symmetric structure, but it has the advantage to provide a global study of both the cluster and the tails that can be easily compared with observational data. In Fig.10 and 11, the volume density of the system is shown at different epochs, for the various orbits. Once the tails have completely developed, outside the S-shape distribution, density clumps appears. They are symmetrically located in the two tails, as shown in Fig.12 for the cluster on quasi-circular orbit: in this case, the most prominent clumps are located at a distance from the cluster center between $0.25r_b$ and $0.4r_b$. The density profiles are very similar to

that of Palomar 5, where clumps are visible in the outer part of the cluster (Odenkirchen et al. 2003).

Of course, the possibility to detect observationally these clumps is strongly related to the cluster position along its orbit. Indeed, we computed the contrast density ratio ρ_{cl}/ρ_*, where ρ_{cl} is the local volume density in the clumps and ρ_* is the background (i.e. the bulge) density around them. This ratio is maximum when the cluster is near apogalacticon and decreases when moving towards perigalacticon, as shown in Table 2. This is due to two complementary effects: when the cluster is near apogalacticon, ρ_* is minimum (according to the galaxy model described in Sect.3.1) and, at the same time, the elongation of the tails tends to compress respect to that at perigalacticon (see, for example, Fig.7 and Fig.8) and so ρ_{cl} increases. If completely detectable, clumps can contain about $7000 M_\odot$ each (i.e. about 10% of the cluster mass at that epoch), as in the case of the cluster moving on the quasi-circular orbit after $30 t_{cross}$.

In order to study the mass distribution along the tails, we have also evaluated the "linear" density for the whole system in the quasi-circular orbit around the galaxy. This study is particularly well fitted to investigate the mass distribution because tails form a long and thin structure. The upper panel of Fig.13 shows the linear mass density as a function of the curvilinear abscissa s along the system: the absolute maximum in the plot corresponds to the cluster location, while the two simmetric relative maxima correspond to the two main clumps. These clumps result to be unbound structures (see also Di Matteo et al. (2004)); we followed the motion of stars that at a certain time stay in the two clumps: they crowd in the clumps for some time and then move away in the outer parts of the tails. Once moved away from clumps, these stars tend to disperse along the cluster tails. Also the simmetric location of these two clumps respect to the cluster center makes improbable that these structures can be due to local disomogenities in the gravitational field along the tails. More probably, these clumps are related to cinematical properties of stars in their surroundings. The bottom panel in Fig.13 shows the derivative of the stellar tangential velocity component with respect to the curvilinear abscissa s defined above. As is evident, the two clumps correspond to a region where this derivative has a negative minimum, which is also the global minimum over the whole extension of the tails. This implies that the local velocity of the stars decreases as they are approaching the clumps, thus leading to the local overdensity which originates such structures. However, the mechanism at the basis of the formation of these structures still requires further and more detailed investigationsd that we postpone to next papers. See, however, the discussion in Miocchi et al. (2004) for the case of clusters in quasi–radial orbits.

4.3. Velocity dispersion

For the two galactic globular clusters M15 and ω Centauri there are observational evidences that the stellar velocity dispersion remains constant at large radii (Scarpa et al. 2003; Drukier et al. 1998).

Three hypotheses have been raised to justify these findings: 1) tidal heating, as suggested by Drukier for M15 (Drukier et al. 1998); 2) the presence of a dark matter halo surrounding the clusters (Carraro & Lia 2000); 3) a breakdown of Newton's law of gravity in the weak acceleration regime (Scarpa et al. 2003).

We studied the velocity dispersion profile of our simulated cluster as it would be detected if the system was seen along a line-of-sight perpendicular to the cluster orbital plane. In Fig.14, line-of-sight velocities of members of the cluster are plotted versus distance from the center, at four different epochs. At $t = 0$, the velocities decrease moving from the center of the cluster outwards, as it is expected from a King model with a tidal cutoff. As the system moves through the galaxy and loses stars, the velocity profile varies significantly: it tends to decrease until a limiting value and then increases again. This behaviour is very similar to that found in M15 (cfr Fig.8 in Drukier et al. 1998).

In Fig.15 the line-of-sight velocity dispersion profile is shown. It is evident from the Figure that in the outer part of the cluster, the dispersion tends to level off. This region corresponds to that characterized by a power-law volume density profile (see Fig.10 and 11). Stars in this region are escaping from the system and their motion is mostly oriented along the radial direction towards the galaxy center. Once escaped, they move around the galaxy weakly interacting with each other, with similar orbital parameters, so that the velocity dispersion found is coherent with that of a set of particles moving in the triaxial potential adopted.

The second relevant finding is the decreasing of the velocity dispersion in the inner part of the cluster, which could be explained by the quick revirialization of the inner part as stellar mass is being lost. This in accordance with the very low velocity dispersion of Pal5 (Odenkirchen et al. 2002), a cluster which has suffered a great mass loss, as it is now well establihed.

5. Results on mass loss

5.1. Mass loss

To estimate the mass loss from the cluster, we decided to use an 'observational' definition. At any given time we compare the cluster local density ρ_{gc} with the background stellar density ρ_*, assuming that a star is actually belonging to the cluster if it is located in a region

dense enough to make it distinguishable from the background, i.e. if

$$\frac{\Delta\rho}{\rho_*} \geq 1, \tag{8}$$

being

$$\Delta\rho = (\rho_* + \rho_{gc}) - \rho_*. \tag{9}$$

The limiting radius r_L is then defined as the radius of the sphere (centered in the cluster density center) in which the cluster 'emerges' from the stellar background. In Fig.16, the evolution of the cluster mass, expressed in units of the initial mass M_0, is shown versus time for all the four simulations performed.

In the case of a cluster moving on orbits with apocenter $\leq 3.5 r_b$, the mass loss is dramatic: after about 30 t_{cross} the cluster loses about 75% of its mass; the best fit of the mass evolution as a function of time is given by:

$$\frac{M(t)}{M(0)} = 0.77 e^{-t/12} + 0.21, \tag{10}$$

where t is expressed in units of the bulge crossing time t_{cross}. In the remaining case, when the orbit extends up to 7.5 r_b, the mass loss rate considerably diminishes and the cluster mass, after 30 t_{cross}, is still about 60% of its initial value. As is evident in Fig.16, in this case the mass loss rate increases every time the cluster passes at the minimum distance from the galaxy center and not all particles which become unbound at perigalacticon are still so while moving again to apogalacticon. It is possible to point out a region around the galaxy center inside which the cluster suffers more of mass loss: in our case (cluster concentration equal to 1.1) this region corresponds roughly to $r \leq 4$ r_b. This conclusion is accordance to what found in Miocchi et al. (2004), where great mass loss occurs for clusters with comparable central density moving on quasi–radial orbits within such region.

Finally, we want to stress that the choice of performing some of the simulations with a reduced number of particles ($N = 1.6 \times 10^4$) did not affect the mass loss rate over the time interval of 30 t_{cross}. Actually, Fig.16 clearly shows that, for the cluster in a quasi-circular orbit, the mass loss rate is the same using either $N = 1.6 \times 10^5$ (solid line) or a ten times smaller N (dashed line).

5.2. Mass segregation and mass function

As explained in Sect.3.2, we adopted mass segregation in the globular cluster initial conditions, for we aim at simulating a dinamically evolved cluster, whose orbit had decayed in the inner galactic region due to dynamical friction. As the cluster begins to lose stars, the

distribution of stars of different masses in the system starts evolving. This is shown in the left column of Fig.17, where the mean mass of stars populating three different spatial regions versus time is plotted. The first region corresponds to the sphere with radius $r = 0.016r_b$ (corresponding to $r = 3.22$ pc, with our choice of M_b and r_b) centered on the cluster, which initially contains 40% of the total mass of the system; the second region is the spherical shell with inner and outer radius $r = 0.016r_b$ and $r = 0.036r_b$ ($r = 7.18$ pc), which initially contains 80% of the cluster mass; the third region is that outside $r = 0.036r_b$. As time passes by, low mass stars begin to escape from the system, and the mean stellar mass in the two inner regions starts to rise, while the external one remains quite constant. The increasing of the mean stellar mass versus time in the central cluster regions is particularly evident in the case of the quasi-circular orbit and of the loop with ellipticity $e = 0.27$, because of the greater mass loss in these two cases. Plotting the mean stellar mass in the three regions defined above as a function of the fraction of mass lost, we see (Fig.17, right column) that the evolution of the mean mass depends mostly on the fraction of mass lost from the system rather than on the number of stars populating the cluster and on the cluster orbital path. The differential mass loss obviously influences the shape of the mass function at different times. In Fig.18 the mass function of stars belonging to the cluster is shown at three different epochs, when the cluster has lost respectively the 20%, the 35% and the 75% of its initial mass. As the cluster loses stars in the galactic field, the mass function evolves towards flatter configurations, because of the preferential loss of low-mass stars, that, accordingly to the initial mass segregation, are located mostly in the external regions of the cluster. The evolution of the mass function appears to be driven by the fraction of mass loss, rather than by other parameters (like the total number of stars in the system and the orbital type of the parent cluster) confirming the findings of Baumgardt & Makino (2003). This is evident from the fact that, for a given fraction of mass lost, the curves found for the different orbits in practice coincide.

6. Conclusions

The main results of our work may be resumed as follows:

1. Stars are lost from the system along a direction which results from the composition of the direction towards the galactic center and the cluster velocity around the galaxy, thus leading to the peculiar S-shape found in the outermost region of the cluster. Once formed, tidal tails are elongated such to remain parallel to the cluster orbit, with a trailing tail that lies slightly inside the orbit and a leading tail slightly outside it. Tails are excellent tracers of the cluster orbit near the pericenter, while, at the apocenter,

they tend to deviate from the orbital path.

2. Tidal tails have a clumpy structure which cannot be associated with an episodic mass loss or tidal shocks with galactic compact sub-structures, since stars are lost from the cluster continuously and since the interaction with the bulge is not episodic. These clumps are not bound self-gravitating systems, they are rather due to a local deceleration of the motion of the stars along the tails.

3. The observational evidence found for M15 and ω Centauri that the velocity dispersion increases and then remains constant at large radii is explained in terms of the so–called 'tidal heating': the stars that evaporate outside the tidal radius of the cluster undergo mainly the interaction with the external field, thus acquiring the higher velocity dispersion pertaining to that field.

7.   Acknowledgement

A.   Adimensionalization of the equations

The equations of motion of the $j-$th star of the cluster, interacting with all the other cluster members and with the bulge are:

$$\ddot{\mathbf{r}}_j = \sum_{i=1}^{N} \frac{Gm_i}{r_{ij}^3} \left(\mathbf{r}_i - \mathbf{r}_j \right) + \nabla U_b \left.\right|_{(x_j,y_j,z_j)} \tag{A1}$$

where $\mathbf{r}_j = (x_j, y_j, z_j)$ is the position vector, r_{ij} is the distance between the $i-$th and the $j-$th particle and U_b is the bulge potential. In the case of the Schwarzschild model (Schwarzschild 1979):

$$U_b(x,y,z) = 4\pi GM_b \left[-\frac{1}{r} \ln\left(\frac{r}{r_b} + \sqrt{1 + (r/r_b)^2} \right) + c_1 \frac{3z^2 - r^2}{2r_b^3 \left(1 + c_2(r/r_b)^2\right)^{3/2}} + \right.$$
$$\left. -3c_3 \frac{x^2 - y^2}{r_b^3 \left(1 + c_4(r/r_b)^2\right)^{3/2}} \right], \tag{A2}$$

where r_b and M_b are the bulge core radius and the bulge mass respectively. Equation (A2) can be rewritten as a product of a dimensional factor and a dimensionless function as:

$$U_b(x', y', z') = 4\pi \frac{GM_b}{r_b} \left[-\frac{1}{r'} \ln\left(r' + \sqrt{1 + r'^2}\right) + c_1 \frac{3z'^2 - r'^2}{2(1 + c_2 r'^2)^{3/2}} + \right.$$
$$\left. -3c_3 \frac{x'^2 - y'^2}{(1 + c_4 r'^2)^{3/2}} \right] \tag{A3}$$

where

$$r' = \frac{r}{r_b}, \quad x' = \frac{x}{r_b}, \quad y' = \frac{y}{r_b}, \quad z' = \frac{z}{r_b}, \tag{A4}$$

Also the first term on the right side of Eq.(A1) can be written as the product of a dimensional factor and a dimensionless one:

$$\sum_{i=1,}^{N} \frac{Gm_i}{r_{ij}^3} (\mathbf{r}_i - \mathbf{r}_j) = G\frac{M_b}{r_b^2} \sum_{i=1,}^{N} \frac{m_i'}{r_{ij}'^3} (\mathbf{r}_i' - \mathbf{r}_j'), \tag{A5}$$

with $m_i' = m_i/M_b$.

Finally, once defined a dimensionless time

$$t' = \frac{t}{t_{cross}}, \tag{A6}$$

being $t_{cross} = (r_b^3/GM_b)^{1/2}$ the bulge crossing time, Eq.A1 may be written as:

$$\frac{d^2\mathbf{r}_i'}{dt'^2} = \sum_{i \neq j}^{N} \frac{Gm_i'}{(r_{ij}')^3} (\mathbf{r}_i' - \mathbf{r}_j') + 4\pi\nabla U'. \tag{A7}$$

This implies that, once assigned the initial conditions $\mathbf{r}_i'(0)$, $\mathbf{v}_i'(0)$, the existence of a unique solution for the Eq. (A7) ensures that all the results obtained can be scaled in terms of the ratios r/r_b, m/M_b and t/t_{cross}.

B.   The construction of multi–mass King model

As described in King (1966), in a single-mass isotropic King model the phase–space stellar distribution function is given by:

$$f(r, v) = \alpha \left[\exp\left(-\frac{E}{m\sigma^2}\right) - \exp\left(\frac{C}{\sigma^2}\right) \right], \text{ if } E \leq -mC \tag{B1}$$
$$= 0 \text{ otherwise}$$

where

$$E = \frac{1}{2}mv^2 + m\psi(r) \tag{B2}$$

is the energy of a star, $\psi(r)$ is the mean gravitational potential generated by the cluster and α is a normalization constant. The 'global' parameter C is related to the tidal radius r_t by the implicit relation

$$\psi(r_t) + C = 0. \tag{B3}$$

The mass density can be found integrating the distribution function $f(r,v)$ over the velocity, obtaining an explicit relation for ρ as a function of the potential ψ:

$$\rho = \int_{E \leq -mC} f(r,v)4\pi v^2 dv = \tag{B4}$$

$$= 4\pi m\alpha e^{C/\sigma^2}(2\sigma^2)^{3/2}\left[-\frac{1}{2}\left(-\frac{\psi+C}{\sigma^2}\right)^{1/2} + \right.$$

$$\left. + \frac{\sqrt{\pi}}{4}\exp\left(-\frac{\psi+C}{\sigma^2}\right)\mathrm{erf}\left(\sqrt{-\frac{\psi+C}{\sigma^2}}\right) - \frac{1}{3}\left(-\frac{\psi+C}{\sigma^2}\right)^{3/2}\right] = \tag{B5}$$

$$= 4\pi m\alpha e^{C/\sigma^2}(2\sigma^2)^{3/2}\left[-\frac{1}{2}\sqrt{-U} + \right.$$

$$\left. + \frac{\sqrt{\pi}}{4}\exp\left(-U\right)\mathrm{erf}\left(\sqrt{-U}\right) - \frac{1}{3}\left(-U\right)^{3/2}\right] = \tag{B6}$$

$$\equiv k\tilde{\rho}\left(U\right) \tag{B7}$$

where $U \equiv (\psi + C)/\sigma^2$ is the dimensionless potential, $k = 4\pi m\alpha e^{C/\sigma^2}(2\sigma^2)^{3/2}$ and $\tilde{\rho}$ is the dimensionless density, which explicitely depends only on U. Once assigned initial conditions for the potential ψ and its derivative ψ' in $r = 0$, the Poisson equation

$$\begin{cases} d^2\psi/dr^2 = 4\pi G\rho, \\ \psi(0) = \psi_0 \\ \psi'(0) = 0 \end{cases}$$

can be rewritten in terms of the dimensionless potential, in the form:

$$\begin{cases} d^2U/d\tilde{r}^2 = 9\rho(U)/\rho(0) = 9\tilde{\rho}(U)/\tilde{\rho}(0) \\ U(0) = U_0 \\ U'(0) = 0 \end{cases}$$

where $\rho(0) = \rho(U_0)$ and $\tilde{r} = r/r_{core}$ being

$$r_{core}^2 = \frac{9\sigma^2}{4\pi G\rho_0} \tag{B8}$$

the King radius.

Once assigned as initial parameters U_0, U_0', the Poisson equation can be integrated, obtaining the dimensionless potential $U(\tilde{r})$, the dimensionless mass density $\tilde{\rho}(\tilde{r})$ and the tidal radius $\tilde{r}_t$, being $\tilde{r}_t = r_t/r_{core}$ with r_{core} yet not determined. To determine the core radius r_{core} and the costant k (which depends, among others, on the normalization constant α), it is possible to procede as follows.
Once assigned as initial parameters the total mass of the cluster M_{tot} and the velocity dispersion σ of stars in the system, using the following relations

$$
\begin{aligned}
M_{tot} &= \int_0^{r_t} 4\pi\rho(r)r^2dr = \\
&= 4\pi k r_{core}^3 \int_0^{\tilde{r}_t} \tilde{\rho}(\tilde{r})\tilde{r}^2 d\tilde{r}
\end{aligned}
\tag{B9}
$$

and the Eq.B8, it is possible to calculate r_{core} and k and hence to obtain $\rho(r)$, r_{core} and $r_t = \tilde{r}_t r_{core}$.

In a multi–mass isotropic King model, as described in Da Costa & Freeman (1976), stars are first grouped in n different mass classes, each characterized by a mass m_i. The phase–space stellar distribution function for the i-th mass class is given by:

$$
\begin{aligned}
f_i(r,v) &= \alpha_i \left[\exp\left(-\frac{E_i}{m_i\sigma_i^2}\right) - \exp\left(\frac{C}{\sigma_i^2}\right)\right], \text{ if } E_i \leq -m_iC \\
&= 0 \text{ otherwise}
\end{aligned}
\tag{B10}
$$

where
$$
E_i = \frac{1}{2}m_iv^2 + m_i\psi(r)
\tag{B11}
$$

is the energy of a star in the i-th mass class, $\psi(r)$ is the mean gravitational potential generated by the *whole* cluster, α_i is a normalization constant and C is related to the cluster tidal radius r_t by Eq.B3. Once again, the mass density for the i-th mass class can be found integrating the distribution function $f_i(r,v)$ over velocities, obtaining an explicit relation for ρ_i in terms of the dimensionless potential U defined above and the ratio σ^2/σ_i^2:

$$
\rho_i = \int_{E_i\leq-m_iC} f_i(r,v)4\pi v^2 dv =
\tag{B12}
$$
$$
= 4\pi m_i\alpha_i e^{C/\sigma_i^2}(2\sigma_i^2)^{3/2}\left[-\frac{1}{2}\left(-\frac{\psi+C}{\sigma_i^2}\right)^{1/2} + \right.
$$
$$
\left. + \frac{\sqrt{\pi}}{4}\exp\left(-\frac{\psi+C}{\sigma_i^2}\right)\text{erf}\left(\sqrt{-\frac{\psi+C}{\sigma_i^2}}\right) - \frac{1}{3}\left(-\frac{\psi+C}{\sigma_i^2}\right)^{3/2}\right] =
\tag{B13}
$$

$$
= 4\pi m_i \alpha_i e^{C/\sigma_i^2} (2\sigma_i^2)^{3/2} \left[-\frac{1}{2}\sqrt{-U\frac{\sigma^2}{\sigma_i^2}} + \right.
$$

$$
+ \left. \frac{\sqrt{\pi}}{4} \exp\left(-U\frac{\sigma^2}{\sigma_i^2}\right) \mathrm{erf}\left(\sqrt{-U\frac{\sigma^2}{\sigma_i^2}}\right) - \frac{1}{3}\left(-U\frac{\sigma^2}{\sigma_i^2}\right)^{3/2} \right] = \tag{B14}
$$

$$
\equiv k_i \tilde{\rho}_i \left(U, \sigma^2/\sigma_i^2\right) \tag{B15}
$$

where $k_i = 4\pi m_i \alpha_i e^{C/\sigma_i^2} (2\sigma_i^2)^{3/2}$ and $\tilde{\rho}_i$ is the dimensionless density. Note that the density profiles ρ_i of the $i-th$ mass class are related to the "global" density distribution ρ by the relation:

$$
\rho(r) = \sum_{i=1}^{n} \rho_i(r). \tag{B16}
$$

To distribute stars in the cluster according to this isotropic multimass King model, we proceeded in the following way:

- Once assigned U_0, U_0', the total cluster mass M_{tot} and the velocity dispersion σ, we integrate the Poisson equation as in the case of a sigle mass model previously described, obtaining the dimensionless potential $U(\tilde{r})$, the "global" mass density ρ, the core radius r_{core} and the tidal radius r_t.

- Then we assigned the mass m_i of stars in the i-th mass class and the total mass $M_{tot,i}$ of each mass class (i.e. $M_{tot,i} = n_i \times m_i$, being n_i the number of stars populating the i-th mass class). In our case, we chose to set the masses $M_{tot,i}$ according to the Salpeter's mass function. For a given value of the ratio σ^2/σ_1^2 (once obtained all the other values according to energy equipartition using the relation $m_1\sigma_1^2 = m_i\sigma_i^2$ for $i \geq 2$), we calculate $\tilde{\rho}_i(U, \sigma^2/\sigma_i^2)$ and then the coefficients k_i using Eq.B9 applied to the $i-th$ mass class.

- We varied the ratio σ^2/σ_1^2 until the relation B16 is satisfied with the desired accuracy.

Finally, stars velocities were generated according to Eq.B10.

C. The GC initial mass function

The GC we considered in our simulations is supposed to have an age of $t_{gc} \sim 10^{9.5}$ yr, thus only stars more massive than ~ 1.2 M$_\odot$ are at that time evolved up to a compact remnant (Straniero et al 1997; Dominguez et al 1999). For this reason, we considered only

stars distributed according to the Salpeter's MF with masses in the range $0.12 \leq m \leq 1.2$ $M_\odot$. Moreover, we assumed that the contribution to the low mass population due to the mentioned remnants is practically negligible.

Indeed, according to the Salpeter's MF, the ratio between the number of remnants whose progenitor had a mass around m_p and the number of stars with mass around m is

$$\frac{N_{\mathrm{remn}}}{N_m} = \left(\frac{m}{m_p}\right)^{2.35}. \tag{C1}$$

Supposing that such progenitors are those giving rise to remnants with mass m, then, from the estimates in Straniero et al (1997) and Dominguez et al (1999), $m_p(M_\odot) \simeq 9.5(m-0.45)$, with $m > 0.45$ $M_\odot$ because stars with lower mass remnants cannot be evolved in a Hubble time. Thus, substituting in Eq. (C1),

$$\begin{aligned} \frac{N_{\mathrm{remn}}}{N_m} &\simeq \left(\frac{0.11 \times m}{m - 0.45}\right)^{2.35} \text{ if } m \geq m_l, \\ &\simeq 0 \text{ otherwise} \end{aligned} \tag{C2}$$

where m_l is the lowest mass a remnant can have at the assumed cluster age. From fitting the above–cited estimates, this lower limit turns out to be $m_l \sim (0.45 \log t_{gc} - 1.2)^{-3.1} + 0.45 \sim 0.59$ $M_\odot$.

One can see that the ratio in Eq. (C2) is monotonically decreasing for $m \geq m_l$, hence the maximum takes place for the lowest mass class we used in the model, i.e. $m = 0.71$ $M_\odot$, for which $N_{\mathrm{remn}}/N_{0.71} \sim 0.05$. Since in our numerical representation $N_{0.71}/N \simeq 0.01$ (N is the total number of particles), then in this class there should have been about $5 \times 10^{-4}N$ remnants. Thus, bearing in mind that the less populated mass class contains $\sim 2 \times 10^{-3}N$, we can reasonably affirm that the MF we assumed for the initial conditions was not substantially affected by stellar evolution neither at the initial time t_{gc} nor later during the simulation (because it lasts much shorter than t_{gc}).

REFERENCES

Aarseth, S.J. 1985, in 'Multiple time scales', Acad. Press, 378

Barnes, J. & Hut, P. 1986, Nature, 324, 446

Baumgardt, H., Makino, J. 2003, MNRAS, 340, 227

Bertola, F., Vietri, M., Zeilinger, W. W. 1991, ApJ, 374, L13

Binney, J., Tremaine, S. 1987, *Galactic Dynamics*, Princeton Univ. Press (Princeton, USA)

Capuzzo Dolcetta, R., Donnarumma, I. 2001, MNRAS, 328, 645

Capuzzo Dolcetta, R., Tesseri, A. 1997, MNRAS, 292, 808

Capuzzo Dolcetta, R., Tesseri, A. 1999, MNRAS, 308, 961

Capuzzo Dolcetta, R., Vicari, A. 2004, submitted to MNRAS(astro-ph/0309488)

Capuzzo Dolcetta, R., Vignola, L. 1997, A&A, 327, 130

Carraro, G., Lia, C. 2000, A&A, 357, 977

Casertano, S., Hut, P. 1985, ApJ, 298, 80

Cohn, H. 1980, ApJ, 242, 765

Combes, F., Leon, S, Meylan, G. 1999, A&A, 352, 149

Da Costa, G. S., Freeman, K. C. 1976, ApJ, 206, 128

de Zeeuw, T., Merritt, D. 1983, ApJ, 267, 571

Dehnen, W., Odenkirchen, M., Grebel, E. K., Rix, H. W. 2004, AJ, 127, 2753

Di Matteo, P., Capuzzo Dolcetta, R., Miocchi, P., 2004, submitted to Celestial Mechanics and Dynamical Astronomy

Djorgovski, S., Piotto, G., Capaccioli, M. 1993, AJ, 105, 2148

Dominguez, I., Chieffi, A., Limongi, M. & Straniero, O. 1997, ApJ, 524-1, 226

Drukier, G. A., Slavin, S. D., Cohn, H. N., Lugger, P. M., Berrington, R. C., Murphy, B. W., Seitzer, P. O. 1998, AJ, 115, 708

Fall, S. M., Zhang, Q. 2001, ApJ, 561, 751

Grillmair C., Pritchet C., van de Bergh S. 1986, AJ, 91, 1328

Grillmair, C. J., Freeman, K. C., Irwin, M., Quinn, P. J. 1995, AJ, 109, 2553

Hénon, M. 1961, Ann.d'Ap., 24, 369

Hernquist, L. & Katz, N. 1989, ApJS, 70, 419

Heggie, D. C., Hut, P. 2003, *The Gravitational Million-Body Problem*, Cambridge Univ. Press (Cambridge, UK)

King, I. R. 1966, AJ, 71, 276

Lehmann, I., Scholz, R.D. 1997, A&A, 320, 776

Lee, K. H., Lee, H. M., Fahlman, G. G., Lee, M. G. 2003, AJ, 126, 815

Leon, S., Meylan, G., Combes, F. 2000, A&A, 359, 907

McLaughlin D. E. 1995, AJ, 109, 2034

Miocchi, P. & Capuzzo-Dolcetta, R. 2002, A&A, 382, 758

Miocchi, P., Capuzzo-Dolcetta, R., Di Matteo, P., & Vicari, A. 2004, in preparation.

Murali, C., Weinberg, M. D. 1997a, MNRAS, 291, 717

Murali, C., Weinberg, M. D. 1997b, MNRAS, 288, 749

Odenkirchen, M., Grebel, E. K., Rockosi, C. M., Dehnen, W., Ibata, R., Rix, H. W., Stolte, A., Wolf, C., Anderson, J. E. Jr., Bahcall, N. A., Brinkmann, J., Csabai, I., Hennessy, G., Hindsley, R. B., Ivezic, Z., Lupton, R. H., Munn, J. A., Pier, J. R., Stoughton, C., York, D. G. 2001, ApJ, 548, L165

Odenkirchen, M., Grebel, E. K., Dehnen, W., Rix, H. W., Cudworth, K. M. 2002, AJ, 124, 1497

Odenkirchen, M., Grebel, E, K., Dehnen, W, Rix, H. W., Yanny, B., Newberg, H. J., Rockosi, C. M., Martínez-Delgado, D., Brinkmann, J., Pier, J. R. 2003, AJ, 126, 2385

Ostriker, J. P. 1985, Dynamics of Star Clusters, J. Goodman and P. Hut, Dordrecht: Reidel, 347

Pesce, E., Capuzzo-Dolcetta, R., Vietri, M. 1992, MNRAS, 254, 466

Salpeter, E. E. 1955, ApJ, 121, 161

Scarpa, R., Marconi, G., Gilmozzi, R. 2003, A&A, 405, L15

Schwarzschild, M. 1979, ApJ, 232, 236

Shapley, H. 1918, PASP, 30, 42

Siegel, M. H., Majewski, S. R., Cudworth, K. M., Takamiya, M. 2001, AJ, 121, 935

Straniero, O., Chieffi, A. & Limongi, M. 1997, ApJ, 490, 425.

Testa, V., Zaggia, S. R., Andreon, S., Longo, G., Scaramella, R., Djorgovski, S. G., de Carvalho, R. 2000, A&A, 356, 127
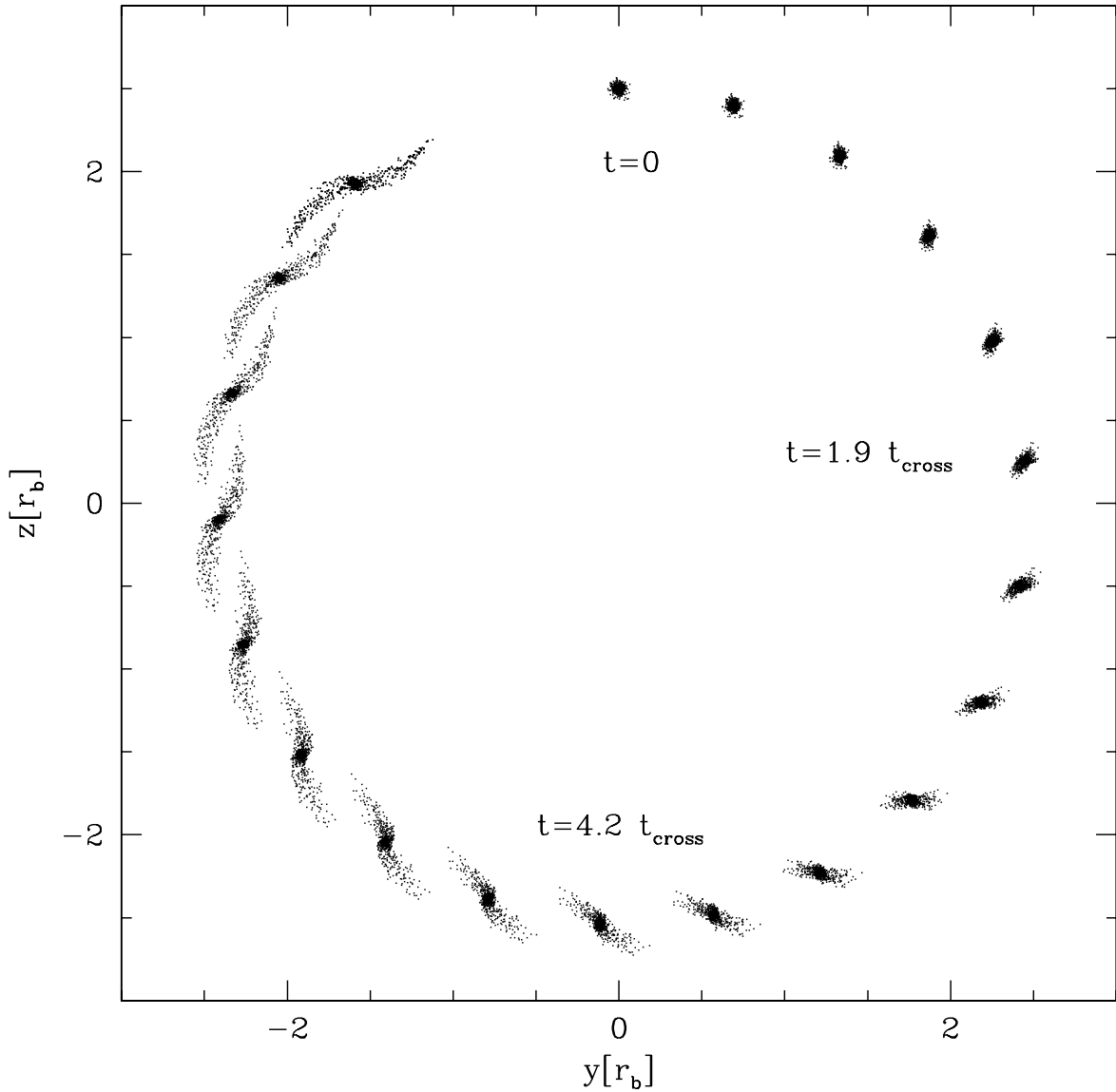
Fig. 1.— First orbital period of a $3 \times 10^5 M_\odot$ globular cluster in the potential described in Sec. 2.2. The cluster moves on a quasi-circular orbit ($e = 0.03$) around the galaxy center in a clockwise direction (see text). Distances are in units of the galactic bulge radius r_b. Some snapshots are labelled with time, expressed in units of the galactic bulge crossing time t_{cross}.
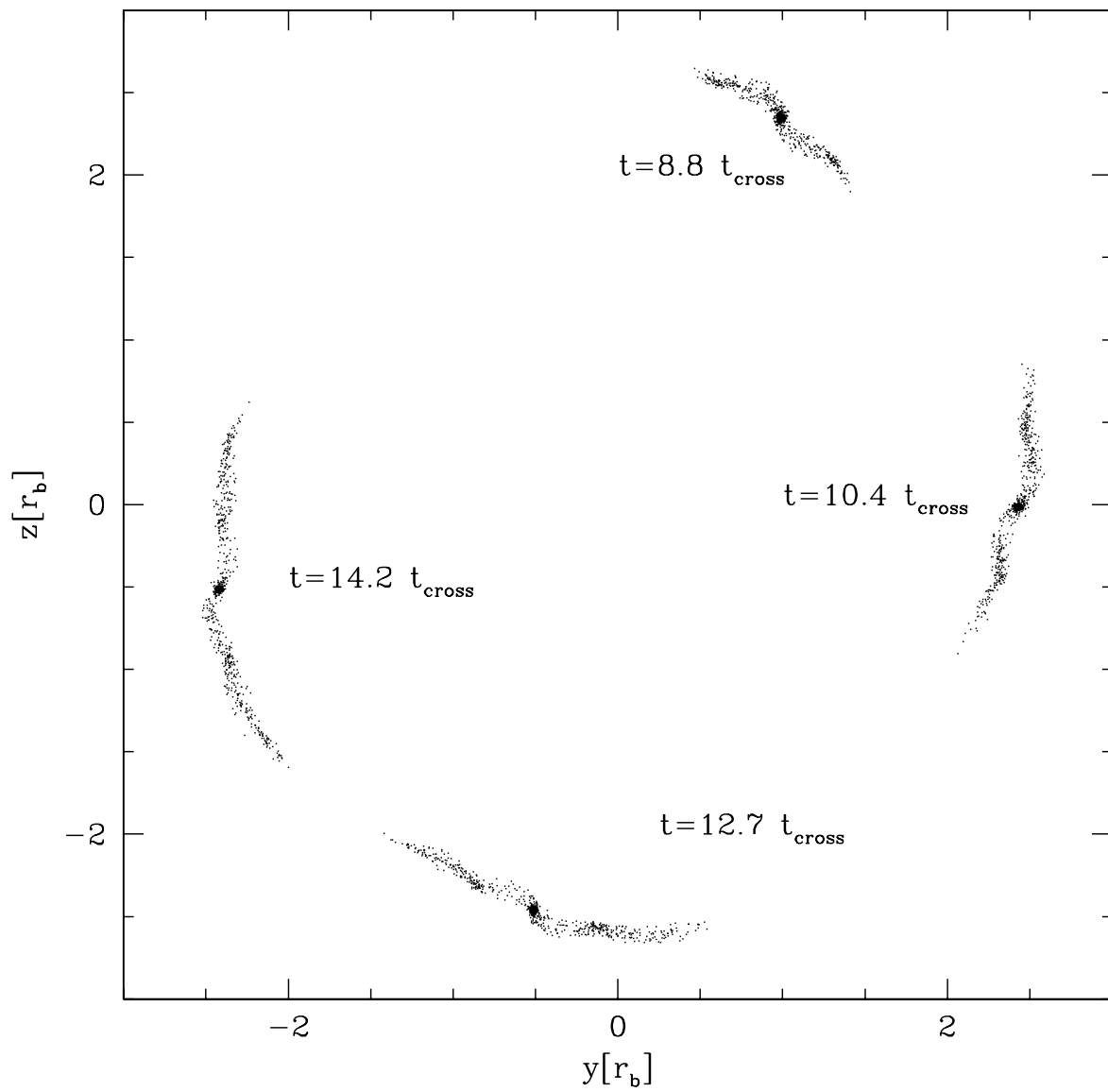
Fig. 2.— Second orbital period of the globular cluster described in the Fig.1.
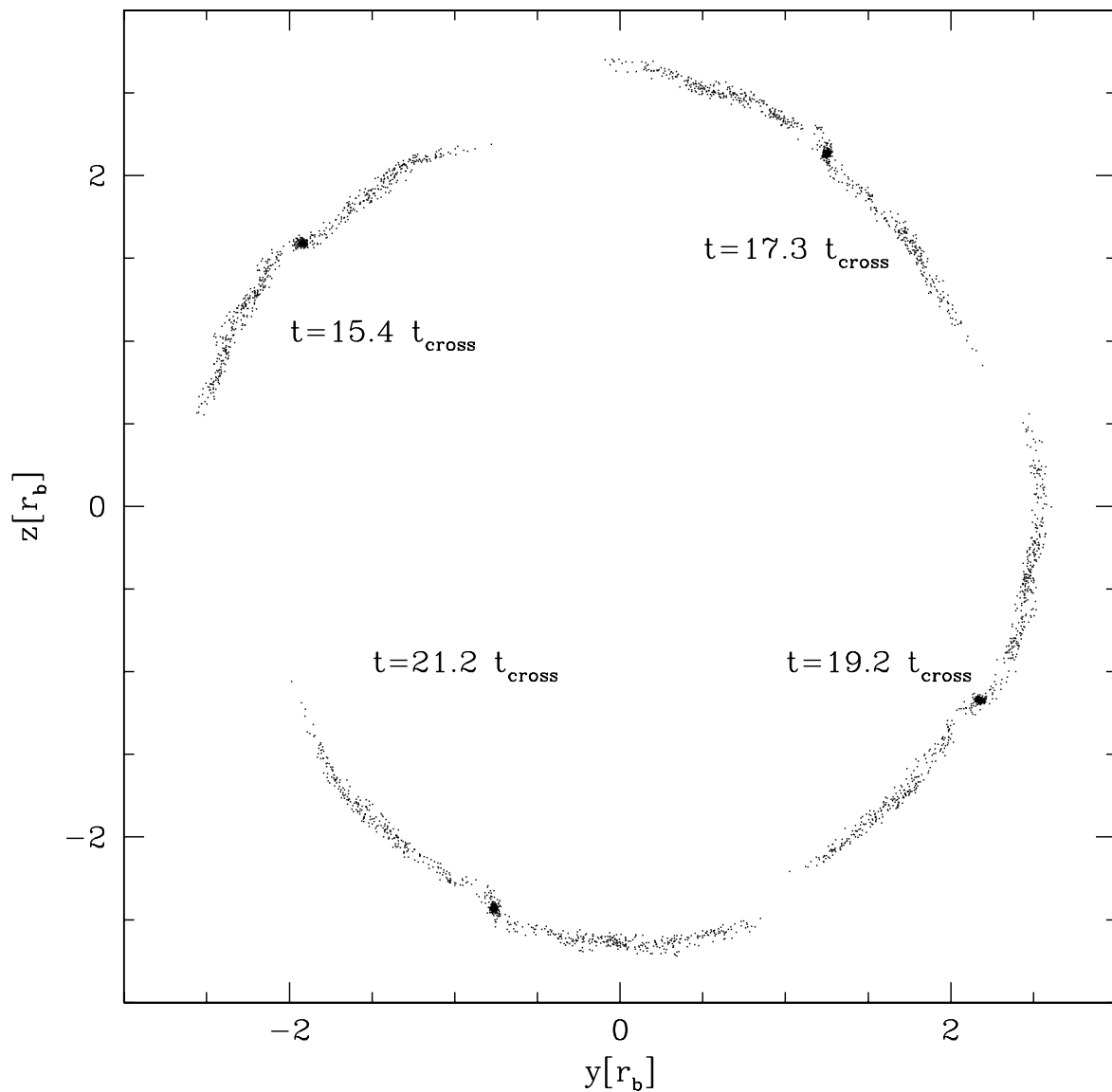
Fig. 3.— Third orbital period of the globular cluster described in the Fig.1.
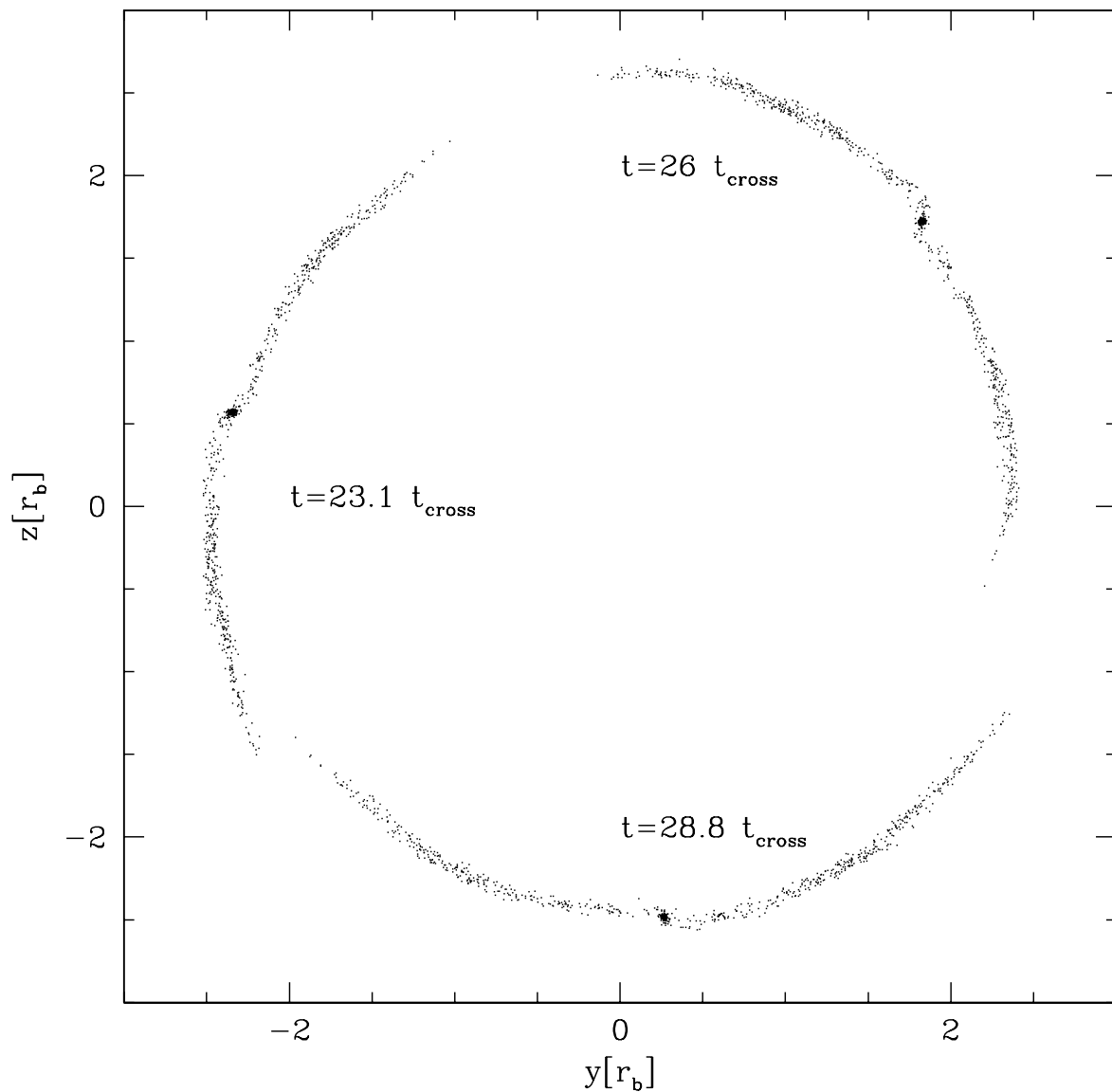
Fig. 4.— Last orbital period of the globular cluster described in the Fig.1.
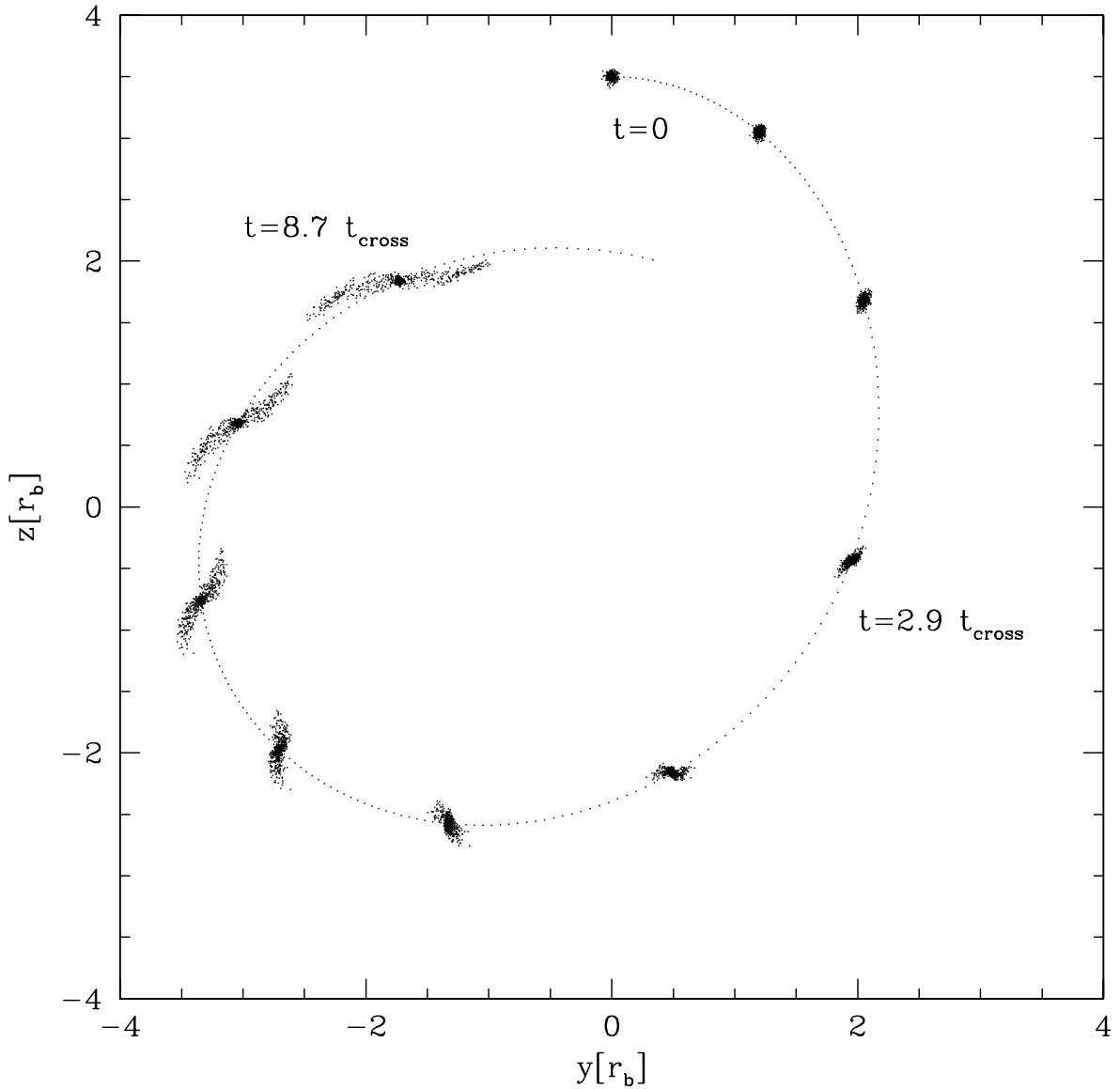
Fig. 5.— First orbital period of the $3 \times 10^5 M_\odot$ globular cluster in a loop orbit with ellipticity $e = 0.27$ around a triaxial galaxy. The cluster moves in a clockwise direction. Some snapshots are labelled with time. The dotted line represents the cluster orbit.
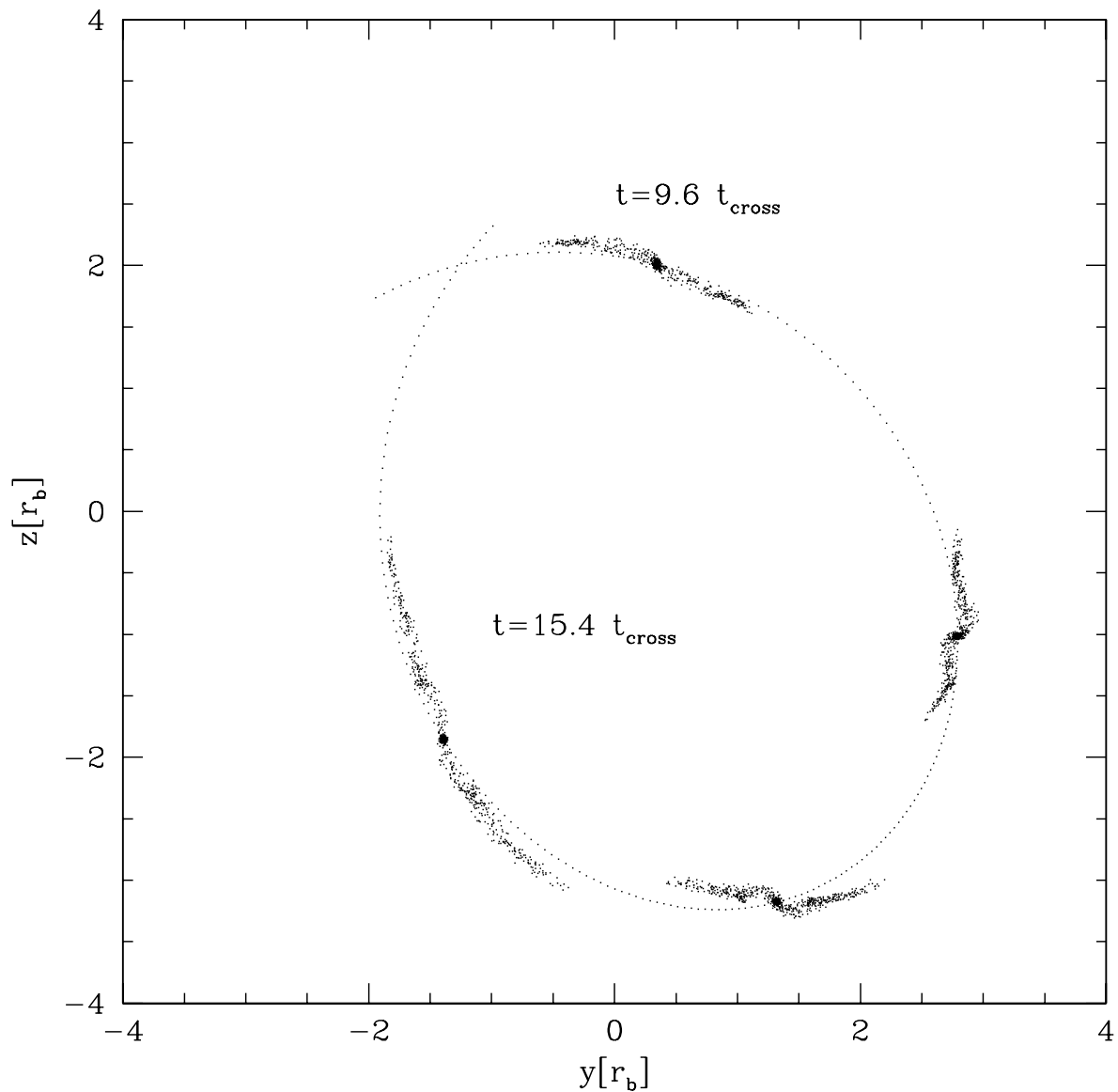
Fig. 6.— Second orbital period of the globular cluster described in the Fig.5.
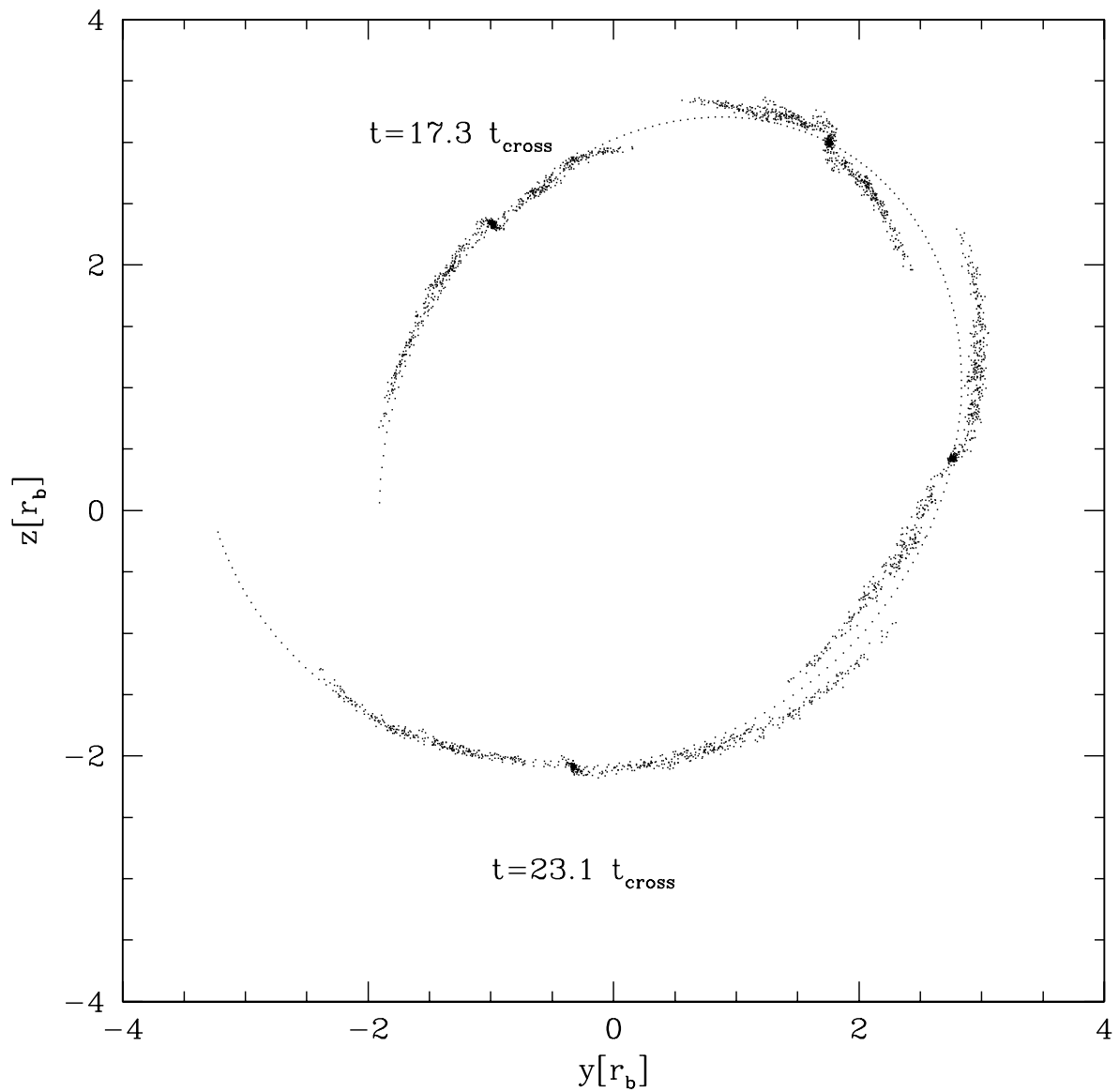
Fig. 7.— Third orbital period of the globular cluster in the Fig.5.
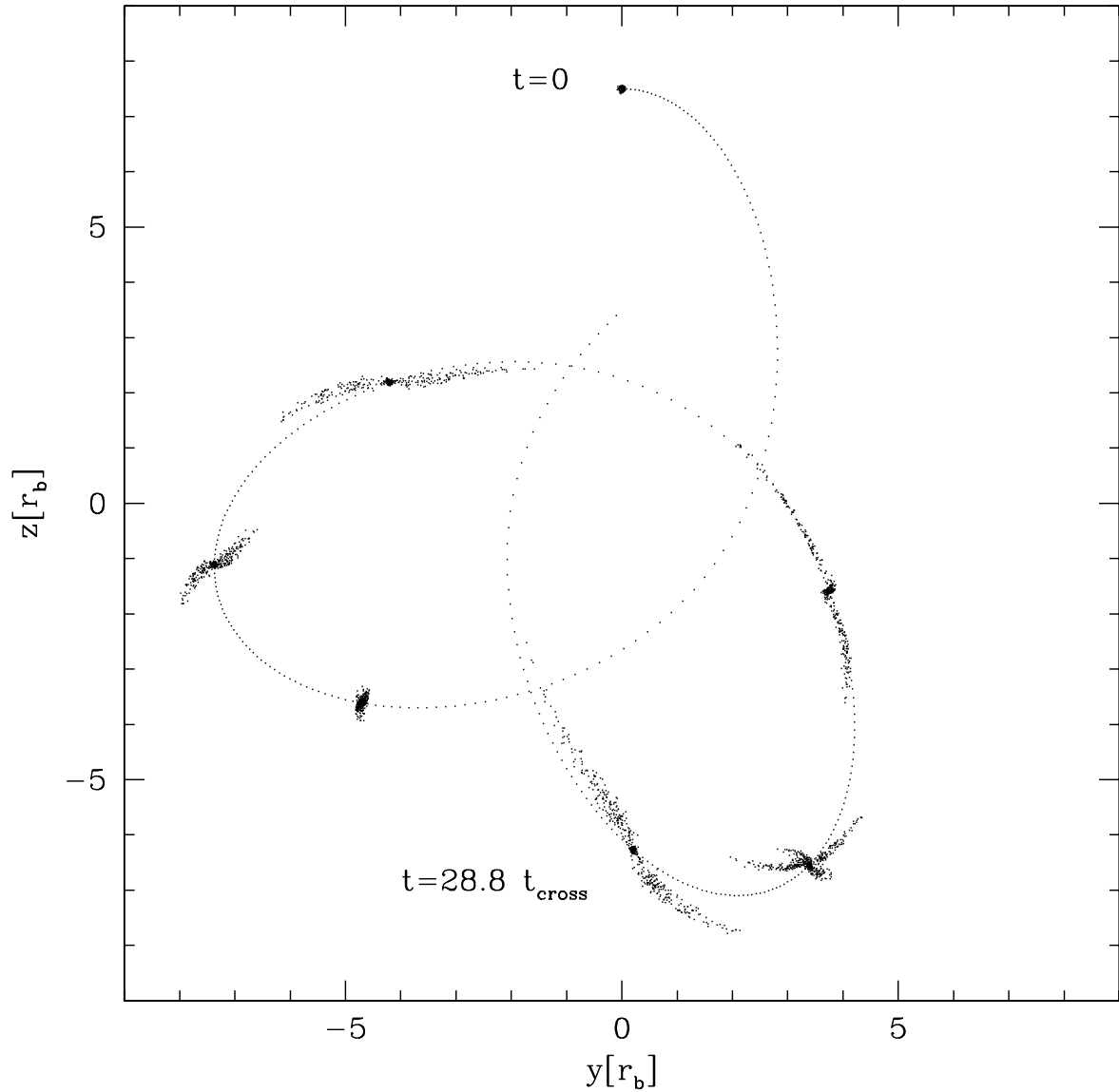
Fig. 8.— Snapshots of the $3 \times 10^5 M_\odot$ globular cluster in a loop orbit with ellipticity $e = 0.57$ around a triaxial galaxy. The cluster moves in a clockwise direction. Some snapshots are labelled with time. The dotted line represents the cluster orbit.
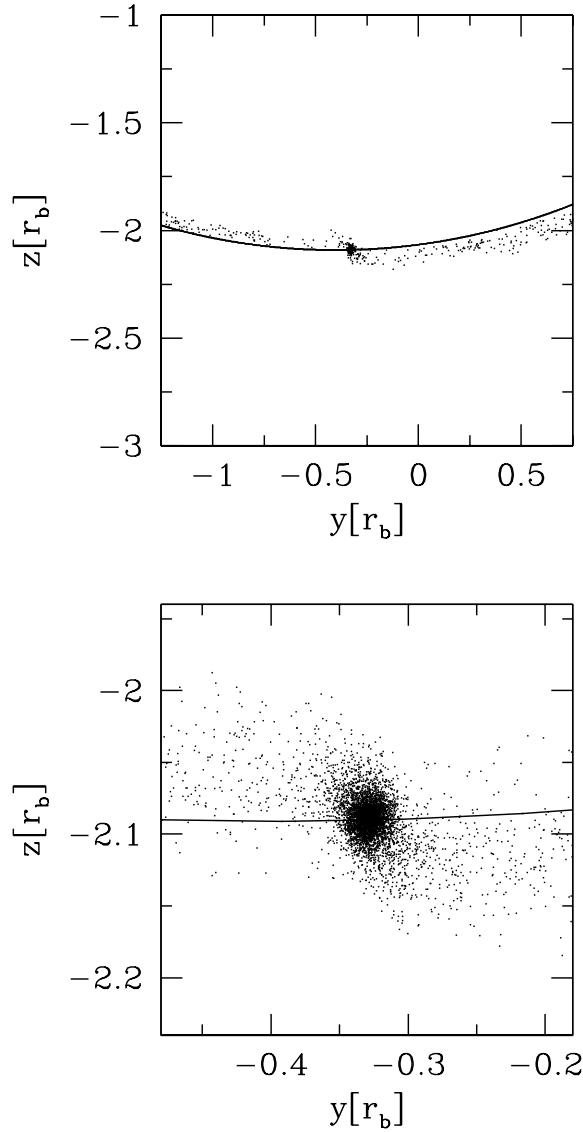
Fig. 9.— Snapshot of the $3 \times 10^5 M_\odot$ globular cluster in the loop orbit with $e = 0.27$ at $t=23.1t_{\mathrm{cross}}$. The upper panel shows the system and the orbit described by the cluster density center (solid line). It is evident from the zoom in the bottom panel that the tails around the cluster core can lead to not reliable information about the orbital path of the cluster (solid line).
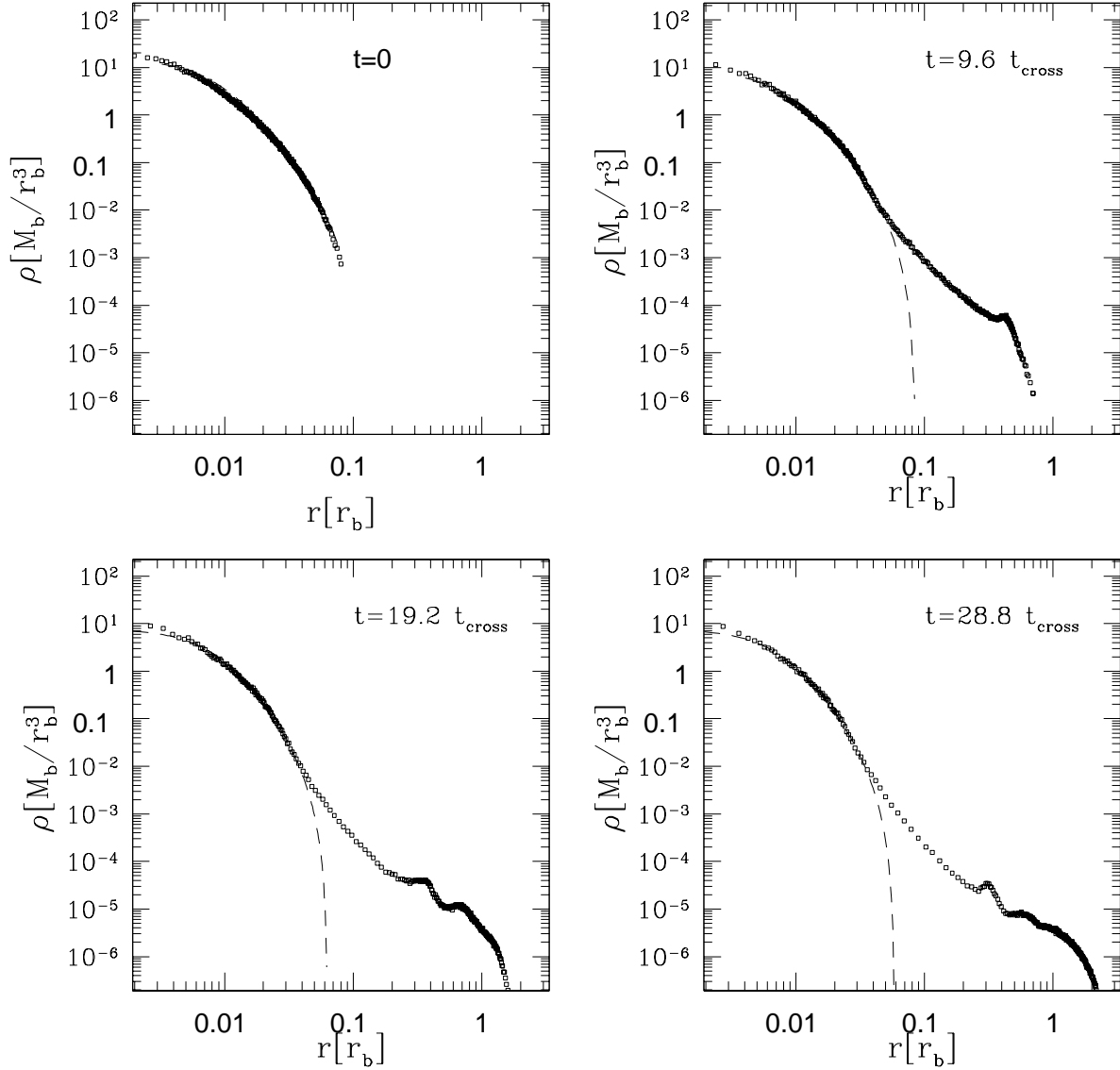
Fig. 10.— Volume mass density of the cluster in the case of the quasi-circular orbit ($e = 0.03$), at four different epochs, as labelled. The dashed line in each panel represents the best King model fit at that epoch. The presence of clumps in the tails are clearly visible.
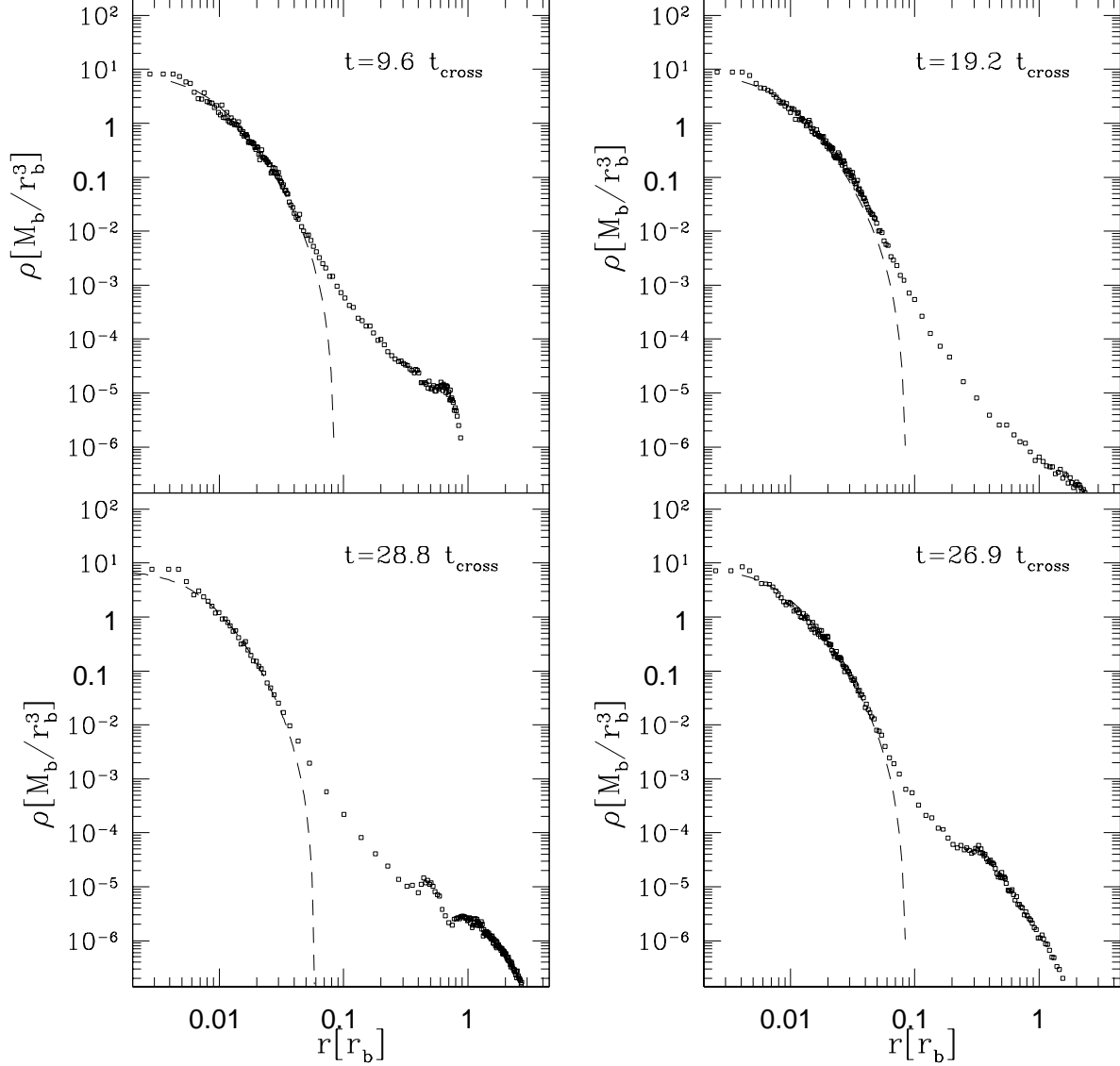
Fig. 11.— Volume mass density of the cluster moving on the loop orbits with $e = 0.27$ (left column) and $e = 0.57$ (right column), at different epochs. The dashed line in each panel represents the best King model fit at that epoch. Note that in the case of most eccentric orbit, clumps are not yet formed at t=$19.2 t_{\rm cross}$.
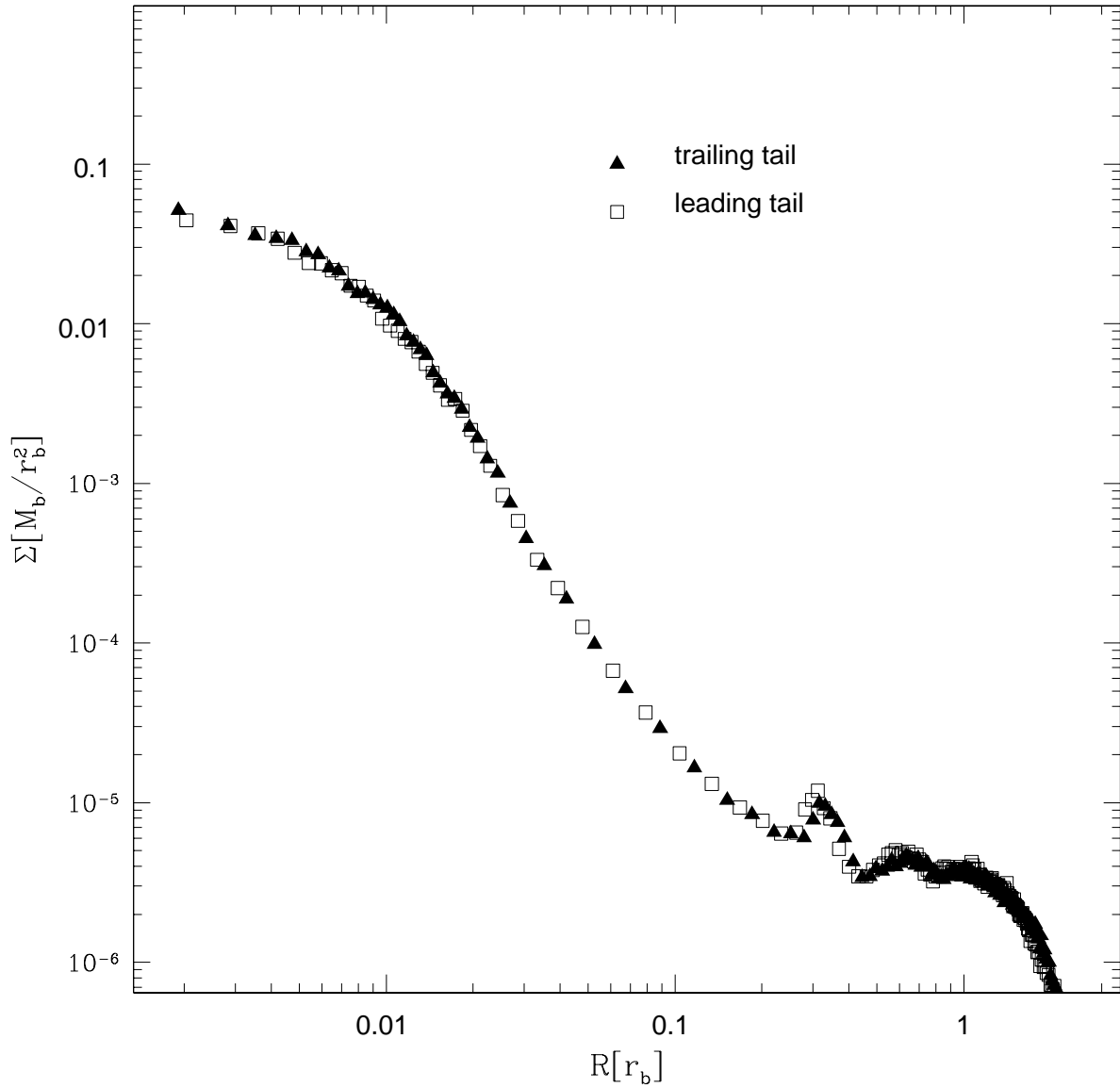
Fig. 12.— Surface density profile of the cluster at t=28.8t_{cross} in the case of the quasi-circular orbit. Two different regions are plotted: that containing the trailing tail (filled triangles) and that containing the leading tail (open squares). The line-of-sight is parallel to the x axis and so perpendicular to the orbital plane.
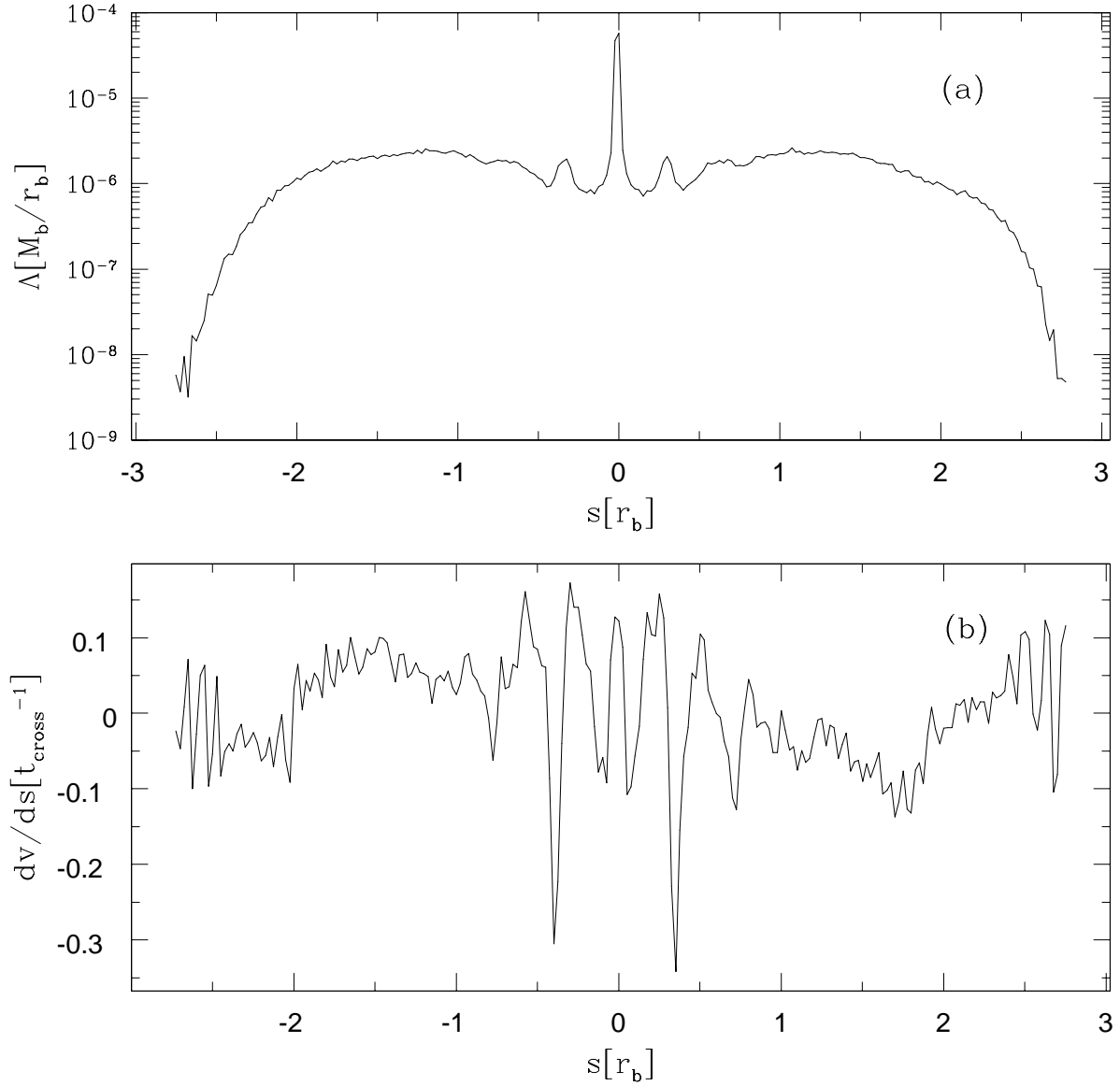
Fig. 13.— Panel (a): Linear mass density as a function of the curvilinear abscissa s, set equal to zero at the cluster center, negative for the traling tail and positive for the leading tail. Panel (b): Derivative of the stellar tangential velocity respect to s.
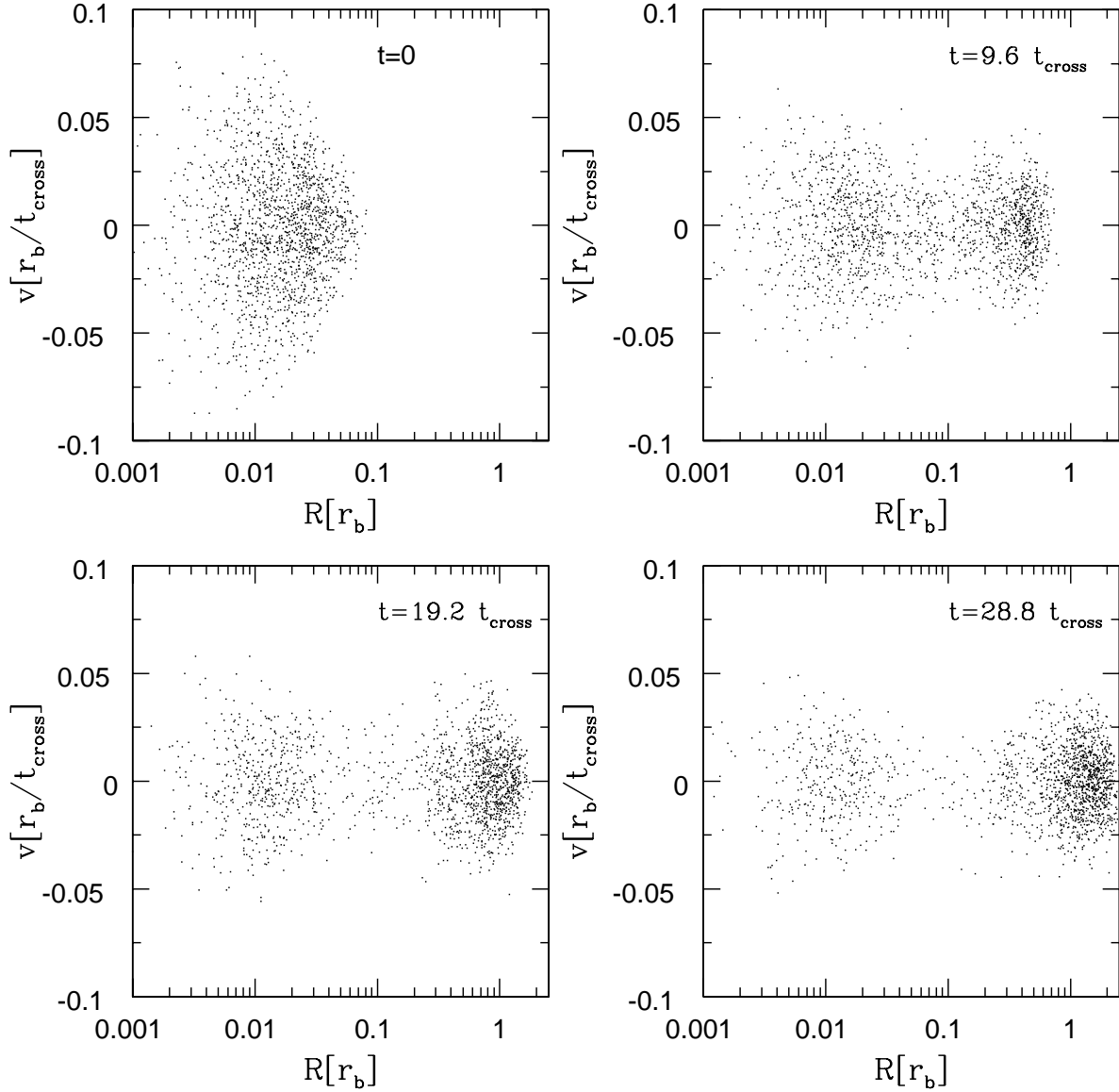
Fig. 14.— Stars velocities along the x axis vs. the distance from the cluster center, for the case of the quasi-circular orbit ($e = 0.03$), plotted at four different epochs. Once stars begin to escape from the cluster, the velocity profile shows a minimum and then increases again.
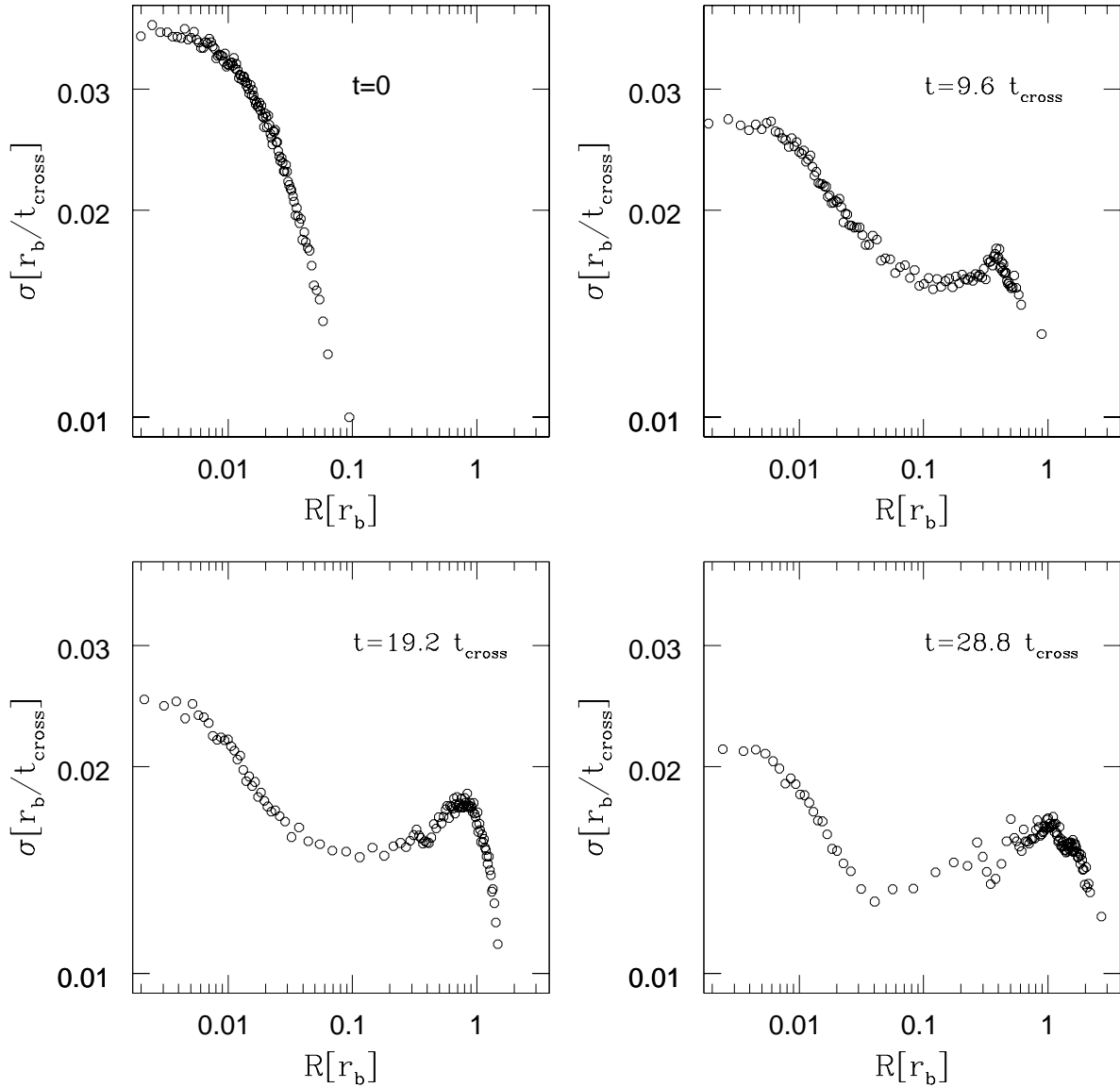
Fig. 15.— Velocity dispersion profiles along the x axis for the cluster in the quasi-circular, at four different epochs.
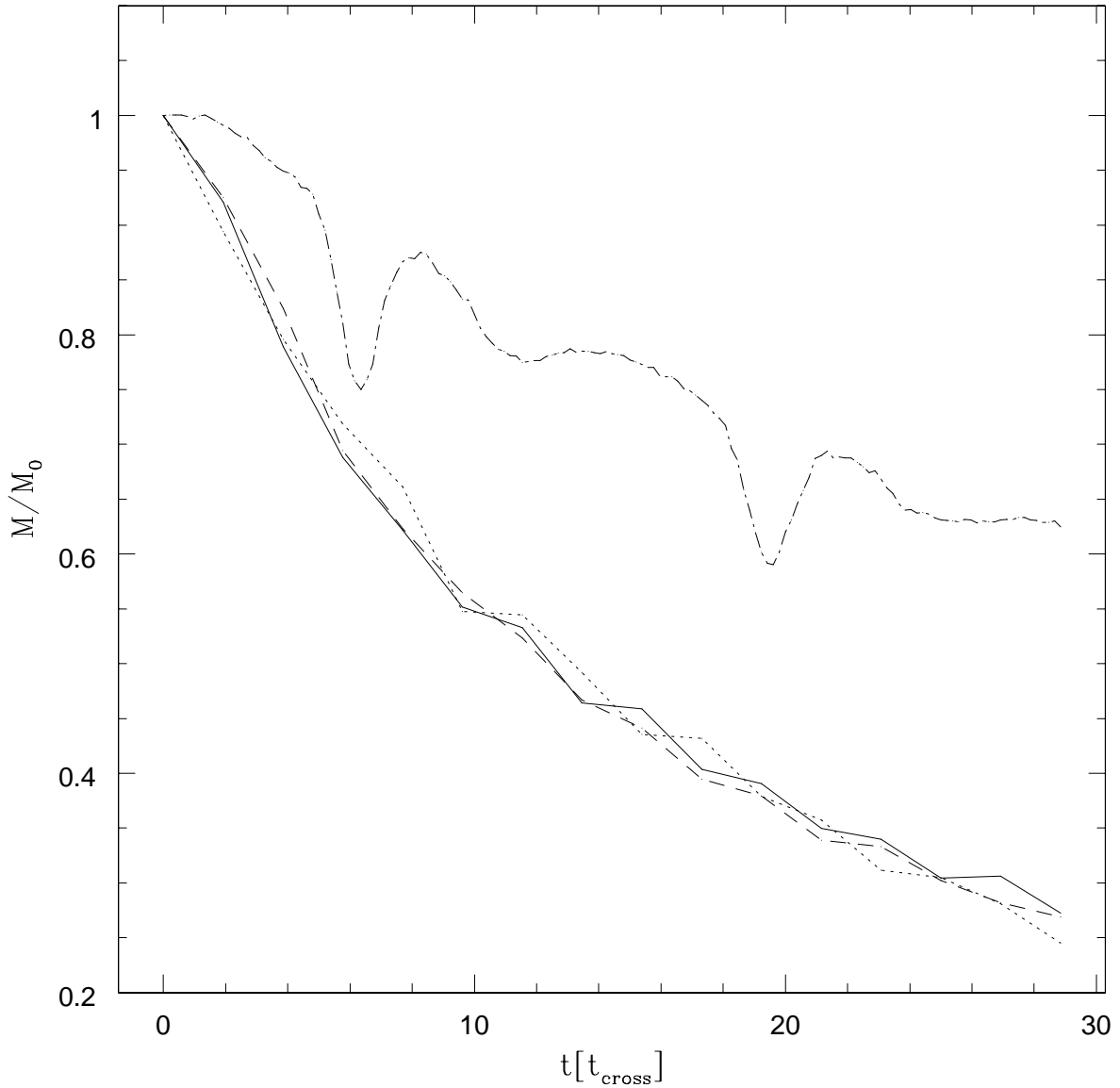
Fig. 16.— Stellar mass belonging to the cluster, in units of the initial cluster mass, as a function of time, expressed in units of the bulge crossing time. Solid line: quasi-circular orbit with $N = 1.6 \times 10^5$ particles. Dashed line: quasi-circular orbit with $N = 1.6 \times 10^4$ particles. Dotted line: loop orbit with $e = 0.27$. Dot-dashed: loop orbit with $e = 0.57$.
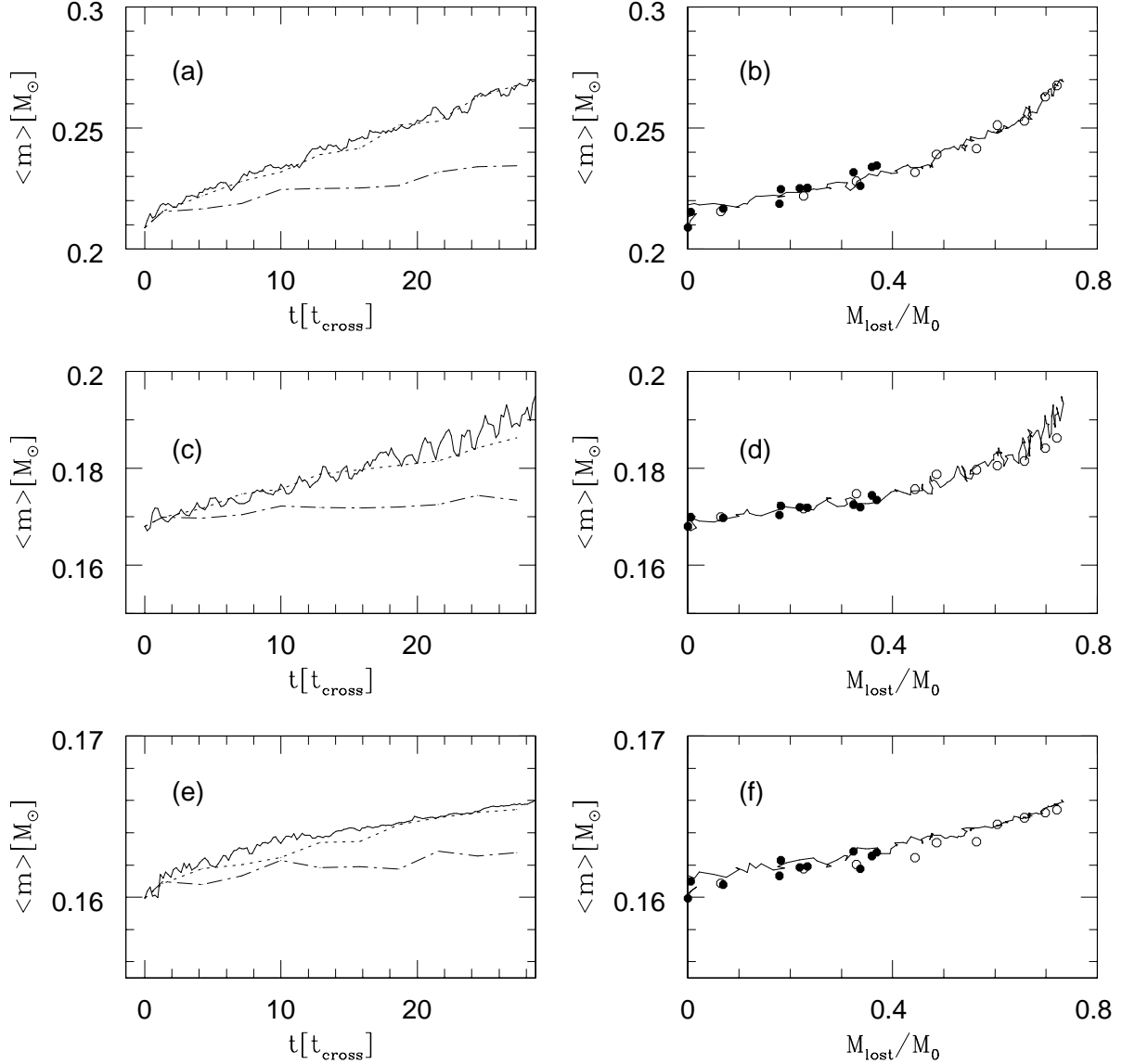
Fig. 17.— Left column: time evolution of the mean mass of stars in three different regions of space centered with the cluster. Panel (a): Mean stellar mass inside $r = 0.016r_b$, in the case of quasi-circular orbit (solid line), loop orbit with $e = 0.27$ (dashed line) and loop orbit with $e = 0.57$ (dot-dashed). Panel (c): Mean stellar mass between $r = 0.016r_b$ and $r = 0.036r_b$. Panel (e): Mean stellar mass outside $r = 0.036r_b$. Right column: evolution of the mean mass of stars in three different regions of space as a function of the fraction of mass lost from the system (in this case both the mass lost and the mean stellar mass have been averaged on time interval of 2.9 t_{cross} for the two loop orbits with greater ellipticities). Panel (b): Mean stellar mass inside $r = 0.016r_b$, in the case of quasi-circular orbit (solid line), loop orbit with $e = 0.27$ (open circles) and loop orbit with $e = 0.57$ (solid circles). Panel (d): Mean stellar mass between $r = 0.016r_b$ and $r = 0.036r_b$. Panel (f): Mean stellar mass outside $r = 0.036r_b$.
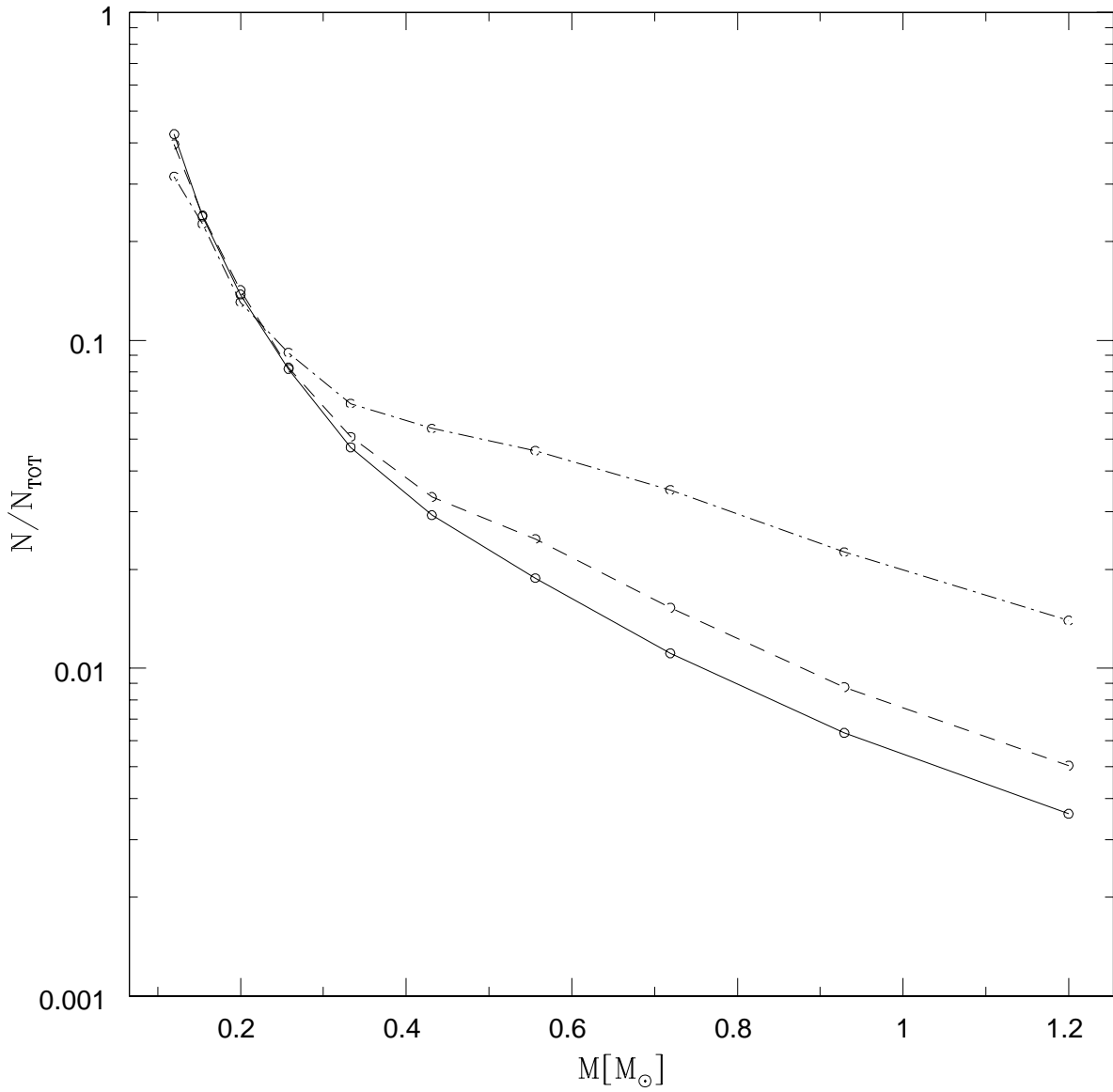
Fig. 18.— Mass function of stars belonging to the cluster at three different epochs: when the cluster has lost the 20% (solid line), the 35% (dashed line) and the 75% of its initial cluster mass (dot-dashed line). Only the evolution of the mass function in the case of quasi-circular orbit is shown, because the other curves (corresponding to orbits with greater ellipticities) coincide with these.

Table 1.   Orbital parameters.

N	e	(x_0, y_0, z_0)	$(v_{x,0}, v_{y,0}, v_{z,0})$
1.6×10^5	0.03	(0,0,2.50)	(0,1.82,0)
1.6×10^4	0.03	(0,0,2.50)	(0,1.82,0)
1.6×10^4	0.27	(0,0,3.50)	(0,1.30,0)
1.6×10^4	0.57	(0,0,7.50)	(0,0.78,0)

Note. — Orbital parameters of the cluster in the four simulations performed. The first column shows the total number of particles used in each simulation. Initial positions and velocities of the cluster with respect to the galaxy center (columns 3 and 4) have been expressed, respectively, in units of the galaxy bulge radius r_b and of the bulge typical velocity dispersion r_b/t_{cross}

Table 2.   Clumps emersion from the background.

$r[r_b]$	ρ_{cl}/ρ_*	$t[t_{cross}]$
2.04	≤ 0.1	9.62
3.44	0.3	13.5
3.47	0.3	19.2
2.12	≤ 0.1	23.1
3.44	0.3	25.0
2.05	≤ 0.1	28.8

Note. — Clumps emersion from the background density, in the case of loop orbit with ellipticity $e = 0.27$. In the first column the cluster distance from the galaxy center is given; the second column shows the ratio between the clumps local density and that of the stellar background; the third column shows the time from the beginning of the simulation, expressed in units of the bulge crossing time.